

# Investigation of physical properties of the $Ce_{1-x}Pr_xCoGe_3$ system

P. Skokowski<sup>a,\*</sup>, K. Synoradzki<sup>a</sup>, M. Werwiński<sup>a</sup>, A. Bajorek<sup>b</sup>, G. Chełkowska<sup>b</sup>, T. Toliński<sup>a</sup>

<sup>a</sup>*Institute of Molecular Physics, Polish Academy of Sciences, Smoluchowskiego 17, 60-179 Poznań, Poland*

<sup>b</sup>*Institute of Physics, Silesian University, Uniwersytecka 4, 40-007 Katowice, Poland*

---

## Abstract

We present the results of our studies of physical properties for the novel  $Ce_{1-x}Pr_xCoGe_3$  system performed with a number of experimental methods: magnetic susceptibility, specific heat, electrical resistivity, magnetoresistance and thermoelectric power. All investigated materials of the  $Ce_{1-x}Pr_xCoGe_3$  series crystallize in the tetragonal  $BaNiSn_3$ -type structure. The lattice parameters and unit cell volume decreases with increasing  $x$ . On the basis of the measurements taken, a tentative magnetic phase diagram was created. A continuous suppression of the long-range magnetic order was observed as the concentration of Pr increase. The critical Pr concentration was determined from linear extrapolation to the lowest temperatures ( $T = 0$  K) and is equal to  $x = 0.66$ .

*Keywords:* Intermetallics, Heavy fermions, Physical properties, RKKY interaction, Kondo interaction, Magnetism

---

## 1. Introduction

Most of the interesting properties of the strongly correlated systems are based on the  $f$  electrons. Extensive experimental and theoretical efforts focus on unconventional superconductivity and effects, like the heavy fermion state, deviations from the Fermi liquid behaviour, and competition between the magnetic RKKY interaction and Kondo effect [1–6]. Some of these physical effects are observed under special conditions, which can be steered by the control parameter  $\delta$  corresponding to the quantity  $|JN_F|$ , where  $J$  is exchange integral and  $N_F$  is the conduction band density of states at the Fermi level  $E_F$  [7]. In most cases  $\delta$  is changed by applying an external magnetic field, hydrostatic pressure or by chemical substitution.

Non-centrosymmetric structures attract scientific interest as the lack of inversion symmetry is the key reason of unconventional superconductivity. One of the widely studied crystal structures is that of  $BaNiSn_3$ -type (space group  $I4mm$ , no. 107). Most of the compounds crystallizing in this structure are composited as  $CeTX_3$ , where  $T$ —transition metal and  $X$ —Si, Ge or Al. The examples are:  $CeRhSi_3$ [8, 9],  $CeIrSi_3$ [10],  $CeRhGe_3$ [11],  $CeIrGe_3$ [12],  $CeCuAl_3$ [13–15] or  $CeAuAl_3$ [16–18]. However, in this group of stoichiometry there are also other types of crystal structures, for example: hexagonal  $BaNiO_3$ -type with representative of  $CeCrGe_3$ [19–21],  $CeTiGe_3$ [22, 23] or  $CeVGe_3$ [24, 25], or orthorhombic  $SmNiGe_3$ -type for  $CeNiGe_3$ [26, 27].

One of most interesting compounds from this group is  $CeCoGe_3$ , with three magnetic phase transitions at

$T_{N1} = 21$  K,  $T_{N2} = 12$  K and  $T_{N3} = 8$  K [28–32]. It also reveals superconductivity under pressure [33, 34] and exhibits a quantum critical point after substitution of Ge with Si [35–37]. Even more complicated magnetism occurs in the system  $CeCo_{1-x}Fe_xGe_3$  [38–40]. In addition, there are several other magnetic compounds based on the stoichiometry  $RECoGe_3$  ( $RE$ —rare earth), for example,  $EuCoGe_3$  [41–44] or  $NdCoGe_3$  [45]. The only exception is  $PrCoGe_3$  - a paramagnetic compound with low values of the electronic specific heat coefficient  $\gamma$  parameter indicating metallic state [45]. The previous investigation of the  $PrCoGe_3$  Fermi surface revealed that in this compound praseodymium behaves identically to lanthanum, as there is no contribution of  $f$  electrons to the Fermi surface [46]. However, justification for this state has not been provided.

The aim of this article was to study an effect of substitution on physical properties of the  $Ce_{1-x}Pr_xCoGe_3$  system and to identify the role of the rare earth element in the magnetism of these alloys. The evolution of magnetism is different than in the previously studied  $CeCo_{1-x}Fe_xGe_3$  system. The energy of RKKY interaction, which is responsible for the magnetic ordering, does not decrease directly as magnetism is rather disturbed as the Pr ions replacing the Ce ions do not contribute to magnetic ordering and they distract the interactions between Ce ions. A similar situation applies to the Kondo interaction, since the Kondo contamination effect occurs for a sample of  $x = 0.8$  and the  $PrCoGe_3$  parent compound exhibits metallic behavior. This is the evidence of a weakening of the Kondo interaction strength with an increase of  $x$ . It also means that there is a Pr concentration threshold, in which magnetism and Kondo lattice are no longer collective in the sample volume. Extensive experimental methods also enabled the explanation of the Pr behaviour in the studied alloys and

---

\*Corresponding author

Email address: przemyslaw.skokowski@ifmpan.poznan.pl (P. Skokowski)

the estimation of the influence of the crystal electric field (CEF) on the properties of the  $\text{Ce}_{1-x}\text{Pr}_x\text{CoGe}_3$  series.

## 2. Methods

### 2.1. Experimental

The polycrystalline samples were obtained by melting high purity elements several times in an arc furnace to ensure the sample homogeneity. final mass loss was less than 1%. finally, the samples ingots were wrapped in tantalum foil, encapsulated in evacuated quartz tubes, and annealed at  $900^\circ\text{C}$  for 7 days.

The crystal structure of prepared samples was investigated with X-ray diffraction measurements performed on X'pert Pro PANalytical device with  $\text{Cu-K}\alpha$  radiation source in room temperature. To test the physical properties of the  $\text{Ce}_{1-x}\text{Pr}_x\text{CoGe}_3$  system, a number of experimental methods were used. As the main measuring device we used a Quantum Design Physical Property Measurement System (QD PPMS) with appropriate options for specific measurements. firstly, the zero field cooling (ZFC) and field cooling (FC) curves of magnetic susceptibility were measured with a vibrating sample magnetometer (VSM) module in the temperature range 2 – 300 K and at applied magnetic field value of 0.1 T. Hysteresis loops were measured at 2 K at magnetic field values up to 9 T. In the next step, specific heat measurements were performed in the temperature range 1.9 – 295 K at the magnetic field value of 0 T and in the range of 1.9 – 40 K for various values of the magnetic field. Further investigation was focused on electrical resistivity and magnetoresistance, which were measured using the four probe method. The resistivity measurements were performed without an applied magnetic field in the range of 2 – 300 K, while magnetoresistance was measured at magnetic field values up to 9 T for temperatures 2 – 30 K. Thermoelectric power data were collected using four probe method of the thermal transport option (TTO) in the temperature range 2 – 300 K. finally, the X-ray photoelectron spectroscopy (XPS) measurements were performed with the use of PHI 5700/660 Physical Electronics spectrometer. The spectra were analyzed at room temperature using monochromatized  $\text{Al K}\alpha$  radiation (1486.6 eV). The clean surface of samples was obtained by *in-situ* fracturing. All procedures and measurements were performed in ultrahigh vacuum chamber (UHV) with base pressure of  $10^{-10}$  Torr.

### 2.2. Calculations

The density functional theory (DFT) calculations of the  $\text{CeCoGe}_3$ ,  $\text{Ce}_{0.5}\text{Pr}_{0.5}\text{CoGe}_3$  and  $\text{PrCoGe}_3$  compositions were carried out using the full-potential local-orbital scheme (FPLO) [48]. We used the experimental lattice parameters [46, 47] and atomic positions [28, 46], see Table 1 and fig. 1.  $\text{CeCoGe}_3$  and  $\text{PrCoGe}_3$  crystallize in a tetragonal non-centrosymmetric structure of the  $\text{BaNiSn}_3$ -type, space group  $I4mm$  [28, 46, 47]. The considered

Table 1: Lattice parameters of  $\text{Ce}_{1-x}\text{Pr}_x\text{CoGe}_3$  compounds.

composition	$a$ (Å)	$c$ (Å)	Ref.
$\text{CeCoGe}_3$	4.32	9.835	[47]
$\text{PrCoGe}_3$	4.308	9.829	[46]
$\text{Ce}_{0.5}\text{Pr}_{0.5}\text{CoGe}_3$	4.314	9.832	interpolated

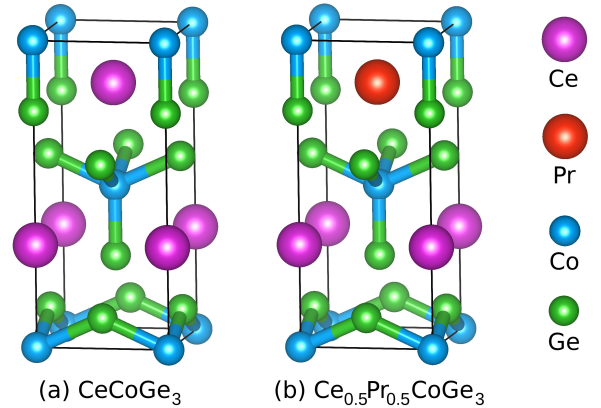


Figure 1: The crystal structure models of (a)  $\text{PrCoGe}_3$  and (b)  $\text{Ce}_{0.5}\text{Pr}_{0.5}\text{CoGe}_3$  compositions. They crystallize in a tetragonal non-centrosymmetric structure of the  $\text{BaNiSn}_3$ -type, space group  $I4mm$  [28, 46, 47].

intermediate composition  $\text{Ce}_{0.5}\text{Pr}_{0.5}\text{CoGe}_3$  was modeled as an ordered compound with one Ce and one Pr atom per unit cell (two formula units), see fig. 1(b). To visualize crystal structures we used the VESTA code [49]. The calculations were performed in a full-relativistic mode within the generalized-gradient approximation (GGA) for exchange-correlation potential in the form of Perdew-Burke-Ernzerhof (PBE) [50] with the FPLO18.00-52 version of the code. We used k-meshes equal to  $20 \times 20 \times 20$  and energy convergence criteria equal to  $2.72 \times 10^{-6}$  eV ( $10^{-7}$  Hartree). For Ce-based compounds with an open Ce  $4f$  shell, it is important to improve the description of local spin density approximation (LSDA) by using e.g. the LSDA plus the U interaction term (LSDA+U). LSDA + U adds Hubbard U intra-atomic repulsion term in energy functional and can significantly improve the LSDA results. A detailed overview of the LSDA+U methods is provided, for example, in the article Ylvisaker *et al.* [51]. For the compositions in question, we used the fully localized limit (FLL) of LSDA+U functional introduced by Czyżyk and Sawatzky [52], sometimes referred also as the atomic limit (AL). The Hubbard U repulsion term introduced in Ce  $4f$  and Pr  $4f$  orbitals was equal 6 eV. This value was calculated previously for Ce [53]. We have also checked that the effect of the on-site repulsion U on the Co  $3d$  orbitals is weak, so the  $U_{3d}$  corrections can be neglected in that case. A similar first-principles approach has been taken to  $\text{PrO}_2$  [54] and other lanthanides systems with

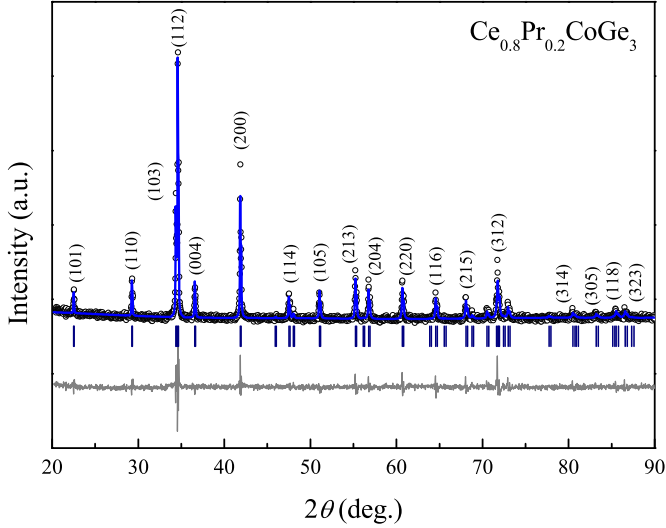


Figure 2: An exemplary XRD pattern of the  $\text{Ce}_{0.8}\text{Pr}_{0.2}\text{CoGe}_3$  ( $x = 0.2$ ) sample. The bottom solid line shows the difference between the measured and calculated patterns. Vertical bars indicate the positions of structural reflections. Miller indices are presented for the most pronounced peaks.

general formula  $\text{LnO}_{1-x}\text{F}_x\text{BiS}_2$ , where  $\text{Ln} = \text{La}, \text{Ce}, \text{Pr}$ , and  $\text{Nd}$  [55]. A similar analysis for isostructural system  $\text{CeCo}_{0.5}\text{Fe}_{0.5}\text{Ge}_3$  have been presented by us [40].

The valence band X-ray photoelectron spectra were calculated based on the band-structure results. The densities of states (DOS) of individual orbitals have been convoluted by the Gaussian function with a full width at half maximum parameter  $\delta$  equal to 0.3 eV. The aim of convolution was to imitate the experimental broadening resulting from the apparatus resolution, lifetime of the hole states and thermal effects. Subsequently, the partial densities of states were multiplied by the appropriate photoionization cross-sections [56].

### 3. Results and discussion

#### 3.1. Crystal structure

The crystal structure of the prepared samples was examined by X-ray diffraction (XRD) measurements at room temperature. The results were analyzed using the FULLPROF[57] program (an exemplary refinement is shown in figure 2) and it revealed that all samples have the desired single-phase non-centrosymmetric tetragonal  $\text{BaNiSn}_3$ -type structure. The crystal lattice parameters are presented in figure 3. Values of the parameters  $a$  and  $c$  and the volume  $V$  decrease with the addition of Pr, as the Pr ion has smaller radius than Ce ion. The ratio  $c/a$  presents small growth of values with the increase of Pr content, suggesting an elongation of the elemental cell.

#### 3.2. Magnetic properties

figure 4 presents temperature dependences of the magnetic susceptibility measured at low temperatures. In part

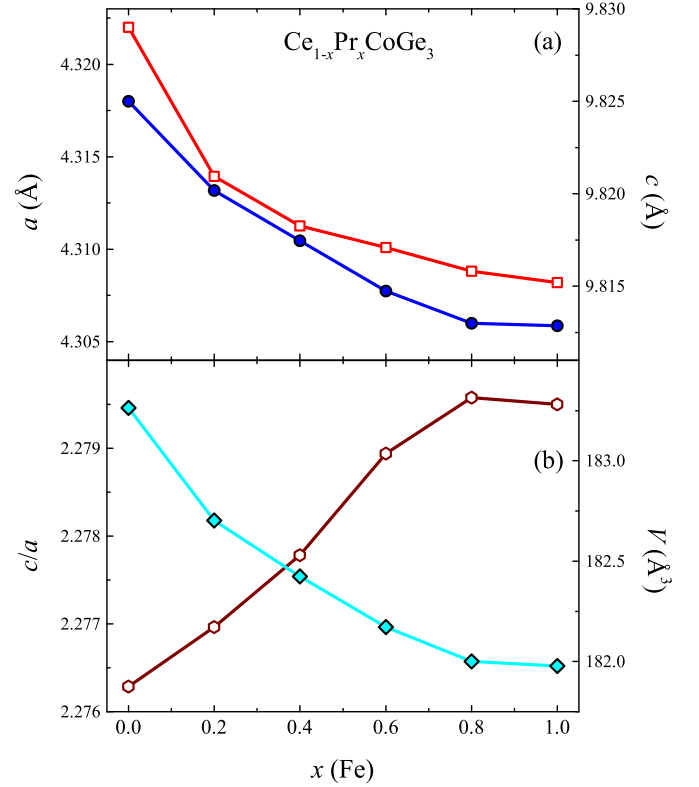


Figure 3: Parameters  $a$  and  $c$  of the crystal lattice, the primitive cell volume  $V$  and the ratio  $c/a$  as function of  $x$  for the series  $\text{Ce}_{1-x}\text{Pr}_x\text{CoGe}_3$ . The solid lines in the figure are guide for the eye.

(a) of figure 4 the sample with  $x = 0.2$  is shown. Similarly as we have done for the series  $\text{CeCo}_{1-x}\text{Fe}_x\text{Ge}_3$ [58], here we denoted the temperatures of phase transitions as  $T_i$  ( $i = 1, 2, 3$ ), as the character of the magnetic ordering may change depending on the range of substitution. The first magnetic transition is shifted to  $T_1 = 12$  K, while  $T_2$  to 8 K and  $T_3$  to 5 K. As for the  $\text{CeCo}_{1-x}\text{Fe}_x\text{Ge}_3$  system, a small amount of substituted element results in the appearance of the ferromagnetic part in the transitions at  $T_2$ . However, a metamagnetic transition is still visible in figure 5 for the magnetization curve of the sample with  $x = 0.4$ . This may suggest that magnetic structure is more or less preserved with the change to ferrimagnetic ordering instead of antiferromagnetic one. This change might be caused by a small difference in cell parameters, which changes the RKKY interaction into a ferromagnetic type or by magnetic disorder, which has a noticeable contribution visible by the large discrepancy between the ZFC and FC curves. In this case, we can assume that the Ce valence is 3, adding  $5d^16s^2$  electrons (neutral electron configuration of Ce is  $[\text{Xe}]4f^15d^16s^2$ ) to the conduction band and with one  $4f^1$  electron entangled to the ion, while the  $\text{Pr}^{3+}$  ion has  $[\text{Xe}]4f^2$  configuration state giving  $4f^16s^2$  electrons (neutral electron configuration of Pr is  $[\text{Xe}]4f^36s^2$ ), resulting in an unchanged number of electrons in the conduction band and thus directly not modifying the RKKY and

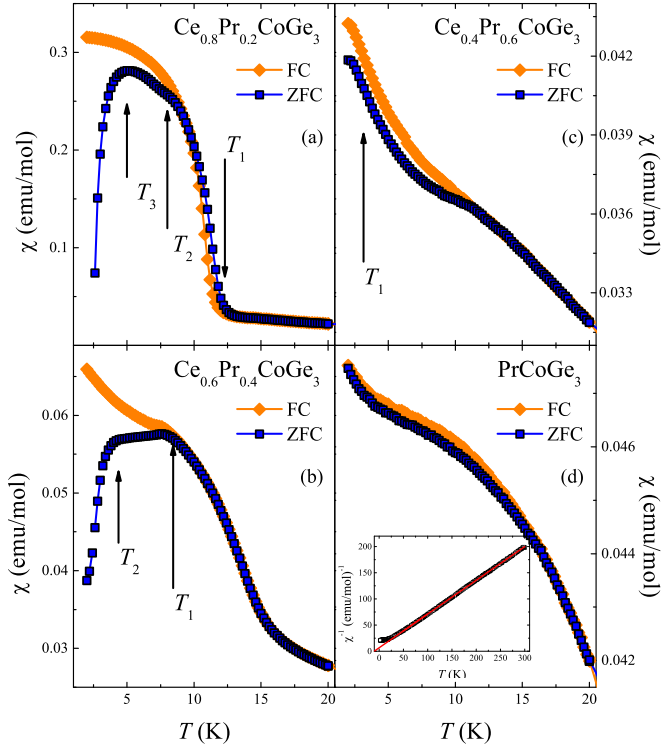


Figure 4: ZFC and FC curves of magnetic susceptibility for the series  $Ce_{1-x}Pr_xCoGe_3$  at  $\mu_0H = 0.1$  T. Inset of (d) is the inverse magnetic susceptibility temperature dependence fitted with the Curie-Weiss law.

Kondo interactions.

For the sample with  $x = 0.4$  the splitting between ZFC and FC curve occurs at  $T_1 = 8$  K, which can be attributed to the phase transition, whereas the next one is at  $T_2 = 3$  K. A broad peak around 12 K is associated with CEF of praseodymium, it is also visible for other samples with  $x \geq 0.6$ . The splitting between ZFC and FC curves also suggests a high disorder in the magnetic structure. In figure 5 there is a small hysteresis with no metamagnetic transition in the measured range of the magnetic field, differently than for the sample with  $x = 0.2$ .

The sample with  $x = 0.6$  also exhibits splitting between ZFC and FC curves. A small hump at  $T = 2$  K implies a possibility of phase transition. Additionally, for this sample the hysteresis is not visible in figure 5. The parent compound  $PrCoGe_3$  shows paramagnetic behaviour with noticeable contribution of CEF, which has been also detected for single crystal case in [100] direction [45].

The denoted temperatures of magnetic phase transitions with usage of magnetic susceptibility results might be inaccurate, because of strong overlapping of the praseodymium CEF contribution. In order to determine temperatures of phase transitions without CEF contribution we used magnetocaloric effect (MCE) isotherms measurements and we calculated the magnetic entropy change

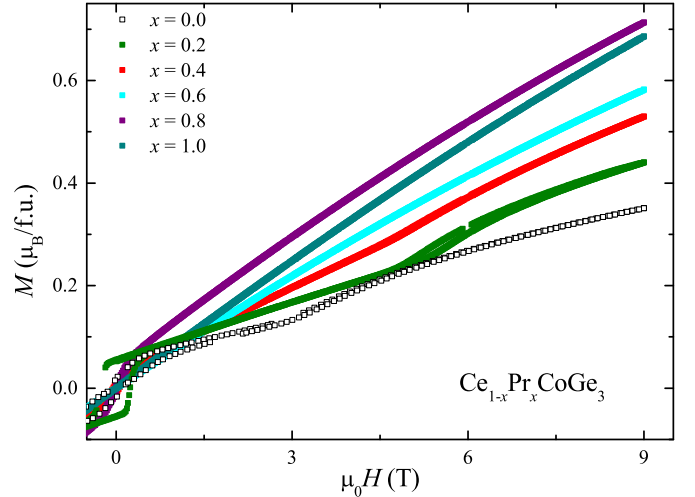


Figure 5: The first quarters of the hysteresis loops for the series  $Ce_{1-x}Pr_xCoGe_3$  at a temperature of  $T = 2$  K

$\Delta S_M$  with formula:

$$\Delta S_M \approx \frac{\mu_0}{\Delta T} \left[ \int_0^{H_{\max}} M(T + \Delta T, H) dH - \int_0^{H_{\max}} M(T, H) dH \right]. \quad (1)$$

Observation of maximum and minimum can designate dominating magnetic ordering[58, 59]. The results of  $\Delta S_M$  in function of temperature for samples with concentrations of  $x = 0.2$  and  $0.4$  are presented in figure 6. The sample with  $x = 0.2$  shows metamagnetic transition at temperature 14.5 K as a maximum for magnetic field value of 9 T. Referring to the magnetic susceptibility results a wide peak is visible at 12 K. Considering similar situation described for  $CeCoGe_3$ [58], the temperature for  $T_1$  transition corresponds to metamagnetic transition resulting in  $T_1 = 14.5$  K. Small hump at temperature 6.5 K and small minimum at 4 K might correspond to temperatures of phase transitions  $T_2$  and  $T_3$  denoted from magnetic susceptibility curves. The all three phase transitions are the same type as  $CeCoGe_3$ [58]. For sample with  $x = 0.4$  there is also maximum with metamagnetic transition at  $T_1 = 8.5$  K, which is corresponding to the observed anomaly in the magnetic susceptibility. A wide peak indicates  $T_2 = 4.5$  K.

Arrott plots for samples with concentration  $x = 0.2$  and  $0.4$  are presented in figure 7. For both samples there is a negative curvature below temperatures  $T_1$ . This suggests a first order metamagnetic transition according to Banerjee criterion [60].

The Curie-Weiss law allowed to determine the valency of Pr in the  $Ce_{1-x}Pr_xCoGe_3$  series. If we assume that the cobalt contribution is negligible, the magnetic susceptibility is a sum of the Ce and Pr contributions with appropriate proportions depending on the stoichiometry

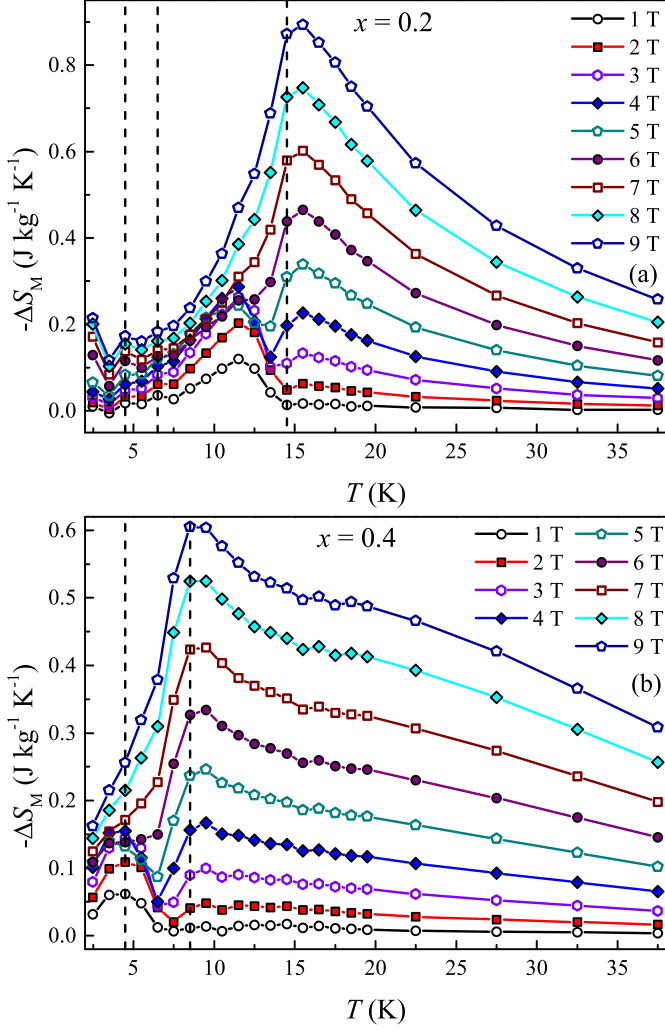


Figure 6: Calculated magnetic entropy change  $\Delta S_M$  in function of temperature  $T$  for  $x = 0.2$  (a) and  $0.4$  (b). The vertical lines indicates the detected phase transitions and anomalies.

Table 2: Data obtained from fitting Curie-Weiss law using the formula:  $\chi(T) = \frac{N_A \mu_{eff}^2}{3k_B(T - \theta_p)} + \chi_0$ , where  $\mu_{eff}^2 = x * \mu_{Pr}^2 + (1-x) * \mu_{Ce}^2$ . Considering previous reports, the cerium effective moment was fixed at  $\mu_{Ce} = 2.54 \mu_B$ .  $\chi_0$  values do not evolve systematically with the increased content of Pr.

$x$ (Pr)	$\mu_{eff}$ ( $\mu_B$ )	$\theta_P$ (K)	$\mu_{Pr}$ ( $\mu_B$ )
0	2.542(2)	-63.7(2)	-
0.2	2.757(7)	-36.6(6)	3.493(7)
0.4	3.035(13)	-24.8(7)	3.653(13)
0.6	3.115(6)	-16.2(3)	3.445(6)
0.8	3.345(13)	-7.7(4)	3.517(13)
1.0	3.519(9)	-10.3(4)	3.519(9)

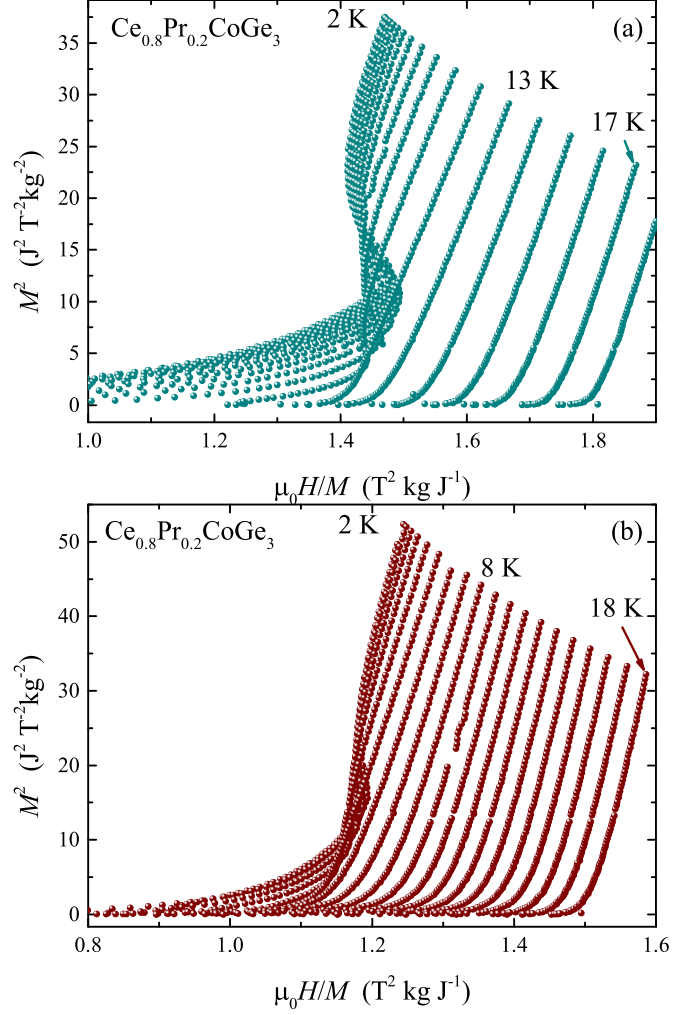


Figure 7: Arrott plots for samples with concentration  $x = 0.2$  (a) and  $0.4$  (b).

of a particular sample. To calculate the magnetic moment of praseodymium  $\mu_{Pr}$ , we used the formula [61]  $\mu_{eff}^2 = x * \mu_{Pr}^2 + (1-x) * \mu_{Ce}^2$  with assumption of value of free cerium  $3+$  ion  $\mu_{Ce} = 2.54 \mu_B$ , as it has been reported previously that in this crystal structure Ce has a magnetic moment value close to  $2.50 \mu_B$ . The data resulting from the fitting of the Curie-Weiss law are presented in Table 1. For all samples, the Pr part of effective moment is around  $3.50 \mu_B$ , which is close to the  $\text{Pr}^{3+}$  ion. The paramagnetic Curie temperature  $\theta_p$  shows a tendency to decrease with increasing  $x$ . This also indicates a reduction in magnetism and strength of Kondo interaction, which finally leads to paramagnetic and metallic type of behaviour for the parent compound  $\text{PrCoGe}_3$ .

### 3.3. Specific heat

Temperature dependences of the specific heat in the temperature range  $1.9 - 40$  K for exemplary samples and different values of the applied magnetic field are presented

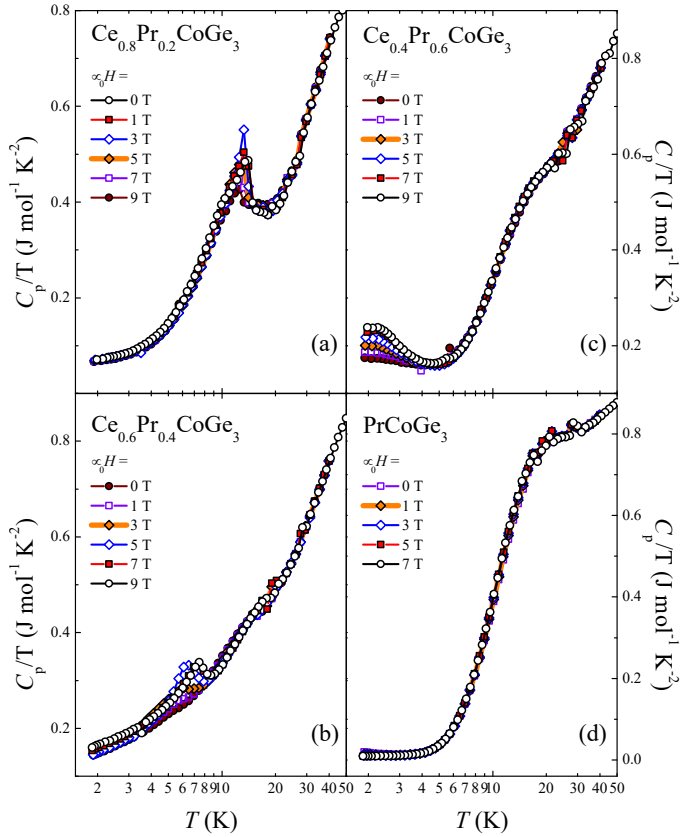


Figure 8: Temperature dependences of the specific heat of  $\text{Ce}_{1-x}\text{Pr}_x\text{CoGe}_3$  samples presented in the form of  $C_p/T$  vs  $\log T$ . Measurements were taken in zero and finite magnetic field.

in figure 8. Values of specific heat for all samples are close to Dulong-Petit limit. The increase in magnetic field values for samples with  $x = 0.2, 0.4$  and  $0.6$  shifts the main peaks connected with the magnetic phase transition  $T_1$  towards lower temperatures, which suggests ferrimagnetic or antiferromagnetic type of ordering. If we consider the results of magnetic susceptibility and isothermal magnetization measurements, we can assume that for these samples the ferrimagnetic ordering scenario is more probable.

The sample with  $x = 0.4$  presents the suppression of the main phase transition  $T_1$  with the increase of the magnetic field values. For the sample with  $x = 0.6$  the transition peak is around 2 K, which is visible owing to the influence of magnetic field on the curves.  $\text{PrCoGe}_3$  provides results similar to those reported earlier [45], with no noticeable changes with the increase of the magnetic field. For all these three samples the CEF contribution connected with praseodymium is visible as a wide peak appearing in the temperature range of 10 – 30 K. In addition, the increase in Pr concentration leads to the distinction of the CEF part. Due to the CEF peak, as well as the magnetic contribution below 12 K, it is difficult to determine the  $\gamma$  parameter values because the correct temperature range cannot be chosen for applying the formula  $C_p/T = \gamma + \beta T^2$ . However, we can observe the trend of the

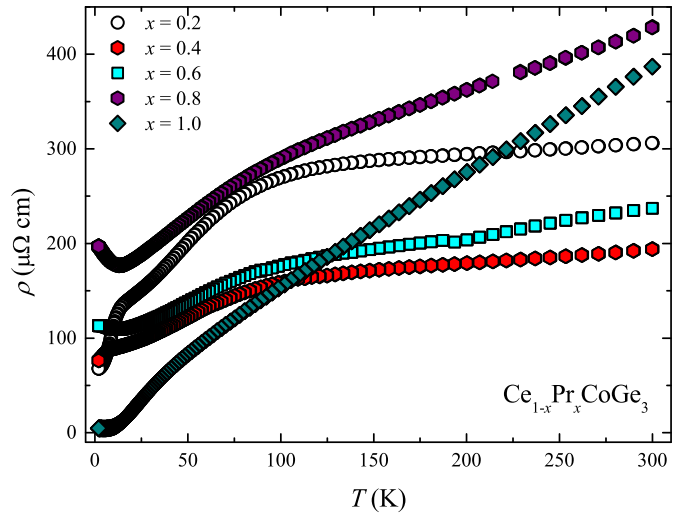


Figure 9: Temperature dependences of the electrical resistivity results for the series  $\text{Ce}_{1-x}\text{Pr}_x\text{CoGe}_3$ .

$\gamma$  values at 2 K. For samples with  $x = 0.2$  and  $0.4$  ( $x = 0.6$  has a phase transition at  $T = 2.2$  K and cannot be considered in the analysis) it can be observed that higher Pr content results in higher  $\gamma$  values, which is rather related to the increase in disorder than to the enhancement of the effective mass and creation of the heavy Fermion state.

### 3.4. Resistivity

The results of the measurements of the temperature dependence of resistivity in the range of 2 – 300 K are shown in figure 9. With increasing concentration of Pr we can observe a clear reduction of the CEF contribution of cerium (broad peak around 100 K) in favor of the praseodymium CEF contribution (around 30 K). This is especially important as we can assume that there are two separate CEF contributions, which are modified by the stoichiometry of the alloy. It is necessary to consider this information in further investigation of the CEF levels for particular alloys of the system  $\text{Ce}_{1-x}\text{Pr}_x\text{CoGe}_3$ .

In figure 9 one can also notice phase transitions for samples with  $x = 0.2, 0.4$  and  $0.6$  at  $T_1 = 12$  K, 7 and 2 K, respectively. For sample with  $x = 0.8$  there is an upturn in the lowest temperatures, which might be connected with a single ion Kondo effect. This is expected as the concentration of Ce is significantly reduced. The threshold between the Kondo lattice and the Kondo impurity effect is between a concentration of  $0.6 < x < 0.8$ , where also the magnetism is suppressed to 0 K.

Similarly as for specific heat results, where CEF contribution of praseodymium and magnetism in the lowest temperatures prevented the systematic calculation of the  $\gamma$  parameter values, the same issues for resistivity do not allow to extract the  $\rho_0$  parameter values. However, we can observe some tendencies, which can provide some rough conclusions. It is noticeable that the overall  $\rho$  values for

alloys at the lowest temperatures increase with the addition of Pr, suggesting a growing chemical disorder (with the exception of the sample with  $x = 0.8$  - it cannot be considered in the analysis as it presents the Kondo impurity effect). For the parent compound  $\text{PrCoGe}_3$ , we observe a metallic type behaviour with a significant CEF contribution in the temperature range of 10 – 30 K. Additionally, the parameter  $RRR = 81$  has rather a high value for a polycrystalline sample. Due to the noticeable disorder visible in the entire substitution range of  $x$  (excluding parent compounds).

### 3.5. Magnetoresistance

To improve the characterization of the magnetic properties of the studied alloys, we have carried out measurements of the resistivity as a function of the magnetic field. In figure 10a we show magnetoresistance plotted as  $MR = [\rho(H, T) - \rho(0, T)]/\rho(0, T)$  for the sample with  $x = 0.2$ . There is a metamagnetic transition reflected as a change from positive to negative values of  $MR$  at temperatures below 12 K and at magnetic field of about 5 T, which confirms that the magnetic structure of  $\text{CeCoGe}_3$  is still maintained for sample with  $x = 0.2$ . Similar behaviour can be observed for the sample with  $x = 0.4$ , but the metamagnetic peak is in the region of negative  $MR$  values, which may suggest a ferrimagnetic ordering with a larger ferromagnetic contribution than in the case of  $x = 0.2$ . For higher temperatures, above 18 K for  $x = 0.2$ , magnetoresistance reveals a wide positive peak, which can be interpreted as the effect of CEF [62]. This is also visible at lower temperatures for samples with  $x = 0.4$  and 0.6. Although the CEF contribution increases with the content of praseodymium, it does not overlap with the magnetic part as the magnetic transitions occur at lower temperatures than the CEF effects. Further increase of temperature causes disappearance of the peak, because we are moving out from the CEF region. A linear, metallic-type form of the positive  $MR$  is revealed.

A more complicated situation is presented in figure 10d, where the parent compound  $\text{PrCoGe}_3$  presents a typical metallic-type  $MR$ , but with high values up to 250%. As metallic behaviour is expected, the source of high  $MR$  values might be not as clear. At first glance, this may be related to the  $MR$  formula and low values of  $\rho_0$ . Looking at the results of other samples and the contribution of the CEF part to  $MR$ , this contribution is not evident in the case of  $\text{PrCoGe}_3$ . Instead, the CEF part is covered by a metallic contribution, unlike for sample with  $x = 0.2$ , where the magnetic contribution is taking this role. Previously, the explanation of the giant  $MR$  in  $\text{Tb}_2\text{Ni}_3\text{Si}_5$  and  $\text{Sm}_2\text{Ni}_3\text{Si}_5$  has been connected with the layered magnetic structure [63]. Additionally, for  $\text{PrNiGe}_3$  compound [64], the authors have suggested the influence of the magnetic field on the mobility of conduction electrons and magnetic ordering. Since the high values of  $MR$  in intermetallic compounds are still not fully explained, we suggest that in our case the interpretation related to the modification of

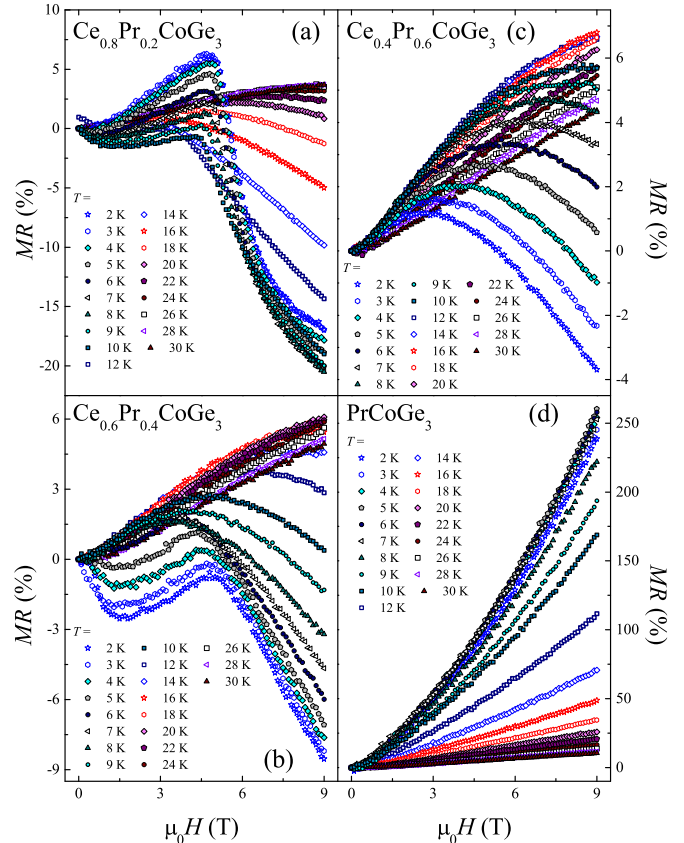


Figure 10: The magnetoresistance isotherms measured in the temperature range 2–30 K for  $x = 0.2, 0.4, 0.6$  and the parent compound  $\text{PrCoGe}_3$ .

electron mobility might be possible. For  $\text{LaCoGe}_3$  [65], the results of  $MR$  are similar to the results  $\text{PrCoGe}_3$ . This is expected because Pr behaves as La in these compounds, providing similar influence on the band structure, as it has been reported by Kawai, *et al.* [46] This may be an indication that the giant  $MR$  for  $\text{PrCoGe}_3$  compound is associated with the band structure and the mentioned modification of the mobility of the conduction electrons.

### 3.6. Seebeck coefficient

In figure 11a the values of the Seebeck coefficient as a function of temperature are presented. A wide peak around 100 K is observed for all samples containing cerium, which is connected with the cerium CEF contribution. The highest value  $S = 43.4(2) \mu\text{V}/\text{K}$  is denoted for sample  $x = 0.2$  at temperature of 95 K. The decrease in maximum values is associated with the decreasing Ce content, whereas the praseodymium CEF contribution visible in range of 10 – 30 K becomes more pronounced with increasing Pr content in alloys. For  $\text{PrCoGe}_3$  very low  $S$  values are observed. However, if we consider the formula  $S = AT + BT^3$ , the linear character of the curve suggests the dominance of the electron diffusion part with almost no contribution of the phonon drag part.

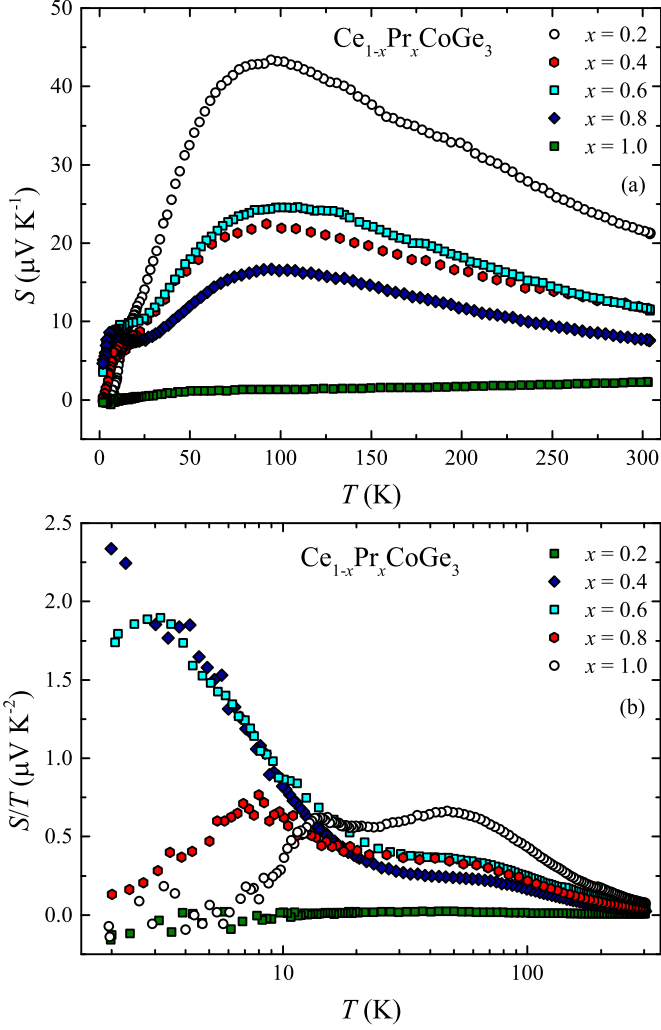


Figure 11: Temperature dependence of the Seebeck coefficient of the  $\text{Ce}_{1-x}\text{Pr}_x\text{CoGe}_3$  samples, plotted in two different representations: (a)  $S$  vs  $T$  and (b)  $S/T$  vs  $\log T$ .

Figure 11b shows the  $S/T$  vs  $\log T$  curves for all samples. Peaks at 12 K, 7 K, and 3 K for  $x$  equal to 0.2, 0.4, and 0.6, respectively, are connected with the magnetic phase transitions. However, the increase in  $S/T$  with decreasing temperature occurs for the concentration of  $x = 0.6$ , which is partially overlapped by the phase transition peak, and for the concentration of  $x = 0.8$ , where the Kondo impurity effect is involved. Observation of this trend may suggest the possibility of NFL behaviour for a very small range of Pr concentration, between regions with magnetic ordering and Kondo impurity, however there are no signs of possible NFL in other experimental results.

### 3.7. X-Ray photoelectron spectroscopy

Exemplary X-ray photoelectron spectra of  $\text{Ce}_{1-x}\text{Pr}_x\text{CoGe}_3$  alloys collected in a wide binding energy range up to 1350 eV with the identification of core levels and Auger lines are shown in figure 12. For all

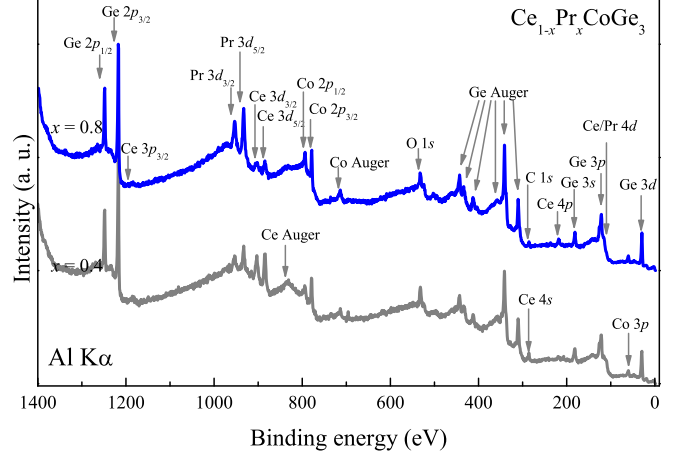


Figure 12: XPS survey spectrum of  $\text{Ce}_{1-x}\text{Pr}_x\text{CoGe}_3$  series for selected samples with  $x = 0.8$  and  $0.4$ .

sample we observed low content of oxygen and carbon, suggesting good quality of the samples received.

For all studied samples the XPS valence bands (VBs) in the energy range 0 – 12 eV are presented in figure 13. In this BE range we observed three broad structures. The broad peak closest to the Fermi level ( $E_F = 0$  eV) is formed by the Pr, Ce ( $5d$ ,  $6s$ ), Co  $3d$ , Ge  $4p$  and Ce  $4f^1$  states. The source of the middle peak ( $\sim 4.0$  eV) is mainly due to the Pr  $4f$  and Ce  $4f^0$  states [66]. Therefore, the position and relative intensity of this peak changes with the change of Ce/Pr concentration. The last structure, broad band of small intensity near 8.0 eV, origin from Ge  $4s$  states. The broadening of all of those peaks is related to the hybridization of conducting electrons and  $4f$  electrons.

In BE region from 90 to 140 eV (figure 14(a)) we observed three sets of spin-orbit split peaks related to Ce  $4d$ , Pr  $4d$ , and Ge  $3p$  states. The positions of the peaks are in good agreement with the ones published for similar systems [67–69]. Additionally, a broad peak assigned to Co  $3s$  state is present at 101.0(1) eV. Due to the overlapping of the Ce  $4d$  spectrum with the Pr  $4d$  and Ge  $2p$  states, nothing can be said about a possible mixed valence of the Ce states. While the relative intensity of the peaks associated with Ge is constant for all samples, the intensity of the peaks associated with Pr and Ce varies significantly for different samples.

The Co  $2p$  XPS spectra for selected samples from  $\text{Ce}_{1-x}\text{Pr}_x\text{CoGe}_3$  series are shown in figure 14(b). The position of the Co  $2p_{3/2}$  and  $2p_{1/2}$  core levels in all investigated samples is around 778.3(1) and 793.4(1) eV, respectively. The Co  $2p_{1/2}$  – Co  $2p_{3/2}$  spin-orbit splitting is about 15.1 eV. The resulting values are practically the same as for pure metallic Co[70]. The lack of additional satellite peaks suggests that there are no Co oxides and that the charge transfer can be neglected in this system. Therefore, the oxidation state of a Co in the  $\text{Ce}_{1-x}\text{Pr}_x\text{CoGe}_3$  series is zero (0). Ge shows a strong peak

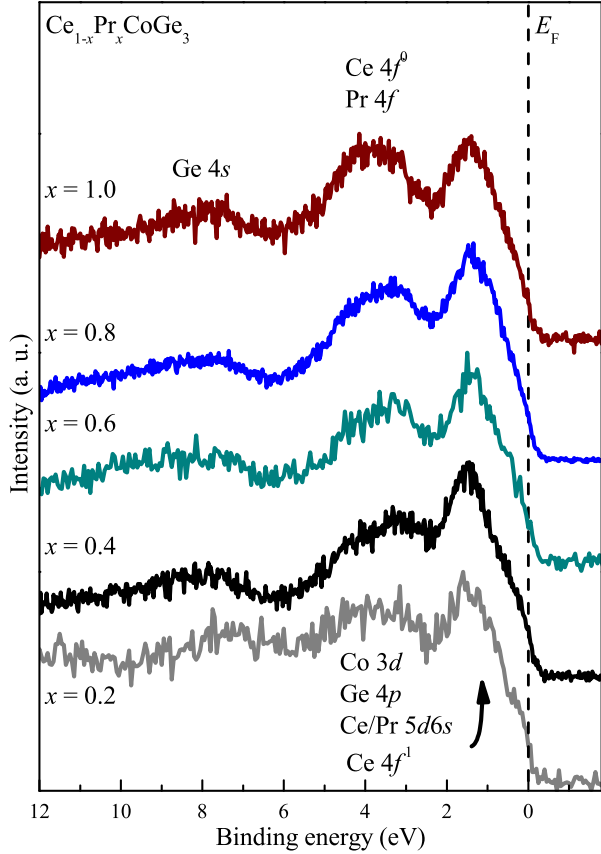


Figure 13: XPS valence band spectra of the  $Ce_{1-x}Pr_xCoGe_3$  series.

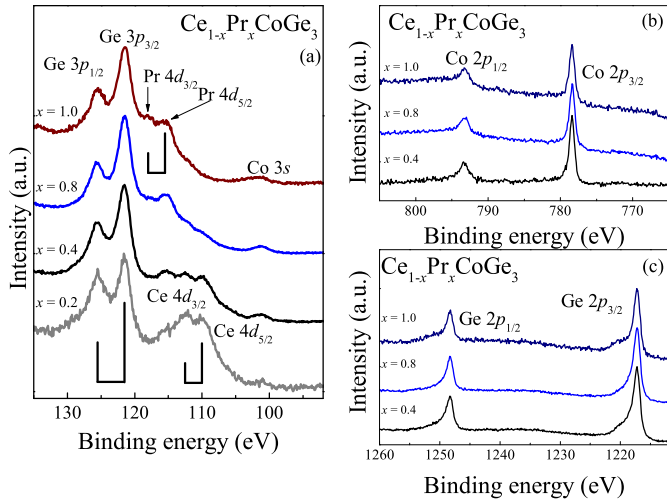


Figure 14: XPS spectrum of the (a) Ge 3p, Ce 4d and Pr 4d, (b) Co 2p, and (c) Ge 2p core levels for the  $Ce_{1-x}Pr_xCoGe_3$  samples.

positions at 1217.3(1) and 1248.3(1) eV, as shown in figure 14(c). The two characteristic peaks correspond to Ge  $2p_{3/2}$  and Ge  $2p_{1/2}$ . Spin-orbit splitting is about 31 eV. In addition to these two sharp peaks, two more wide satellites have been registered towards higher BE. These structures probably come from Ge oxide [71].

figures 15 and 16 present  $3d$  states of Ce and Pr for selected samples of  $Ce_{1-x}Pr_xCoGe_3$  series. In all cases we observed set of two broad peaks which originates from spin-orbit splitting of  $3d$  states. The spin-orbit splitting is equal to 18.7(1) and 20.4(1) eV for Ce and Pr, respectively. The resulting spectra for Pr look very similar to those published for pure Pr and other compounds containing Pr [72–74]. No visible changes in the Ce and Pr  $3d$  spectra have been observed with the change in concentration  $x$ . Analysis of XPS spectra for states  $3d$  Ce and Pr can provide useful information about valence state and hybridization strength. Therefore, we used Gunnarsson-Schönhammer theory to describe these spectra [75, 76]. The exemplary analysis of the Ce  $3d$  and Pr  $3d$  XPS spectra are presented in figure 15 for  $Ce_{0.8}Pr_{0.2}CoGe_3$  and figure 16 for  $Ce_{0.6}Pr_{0.4}CoGe_3$ , respectively. To model the background, the Tougaard algorithm was used [77]. Relative small values of the intensity ratio  $r_2 = I(f^2)/[I(f^1) + I(f^2)]$ , implicates weak electron hybridization. Moreover, the absence of clear peaks from the Ce  $4f^0$  states clearly indicates a full occupancy of the  $f$  orbital. In order to get the best possible fittings, it was necessary to include additional peaks (dotted lines in figure 15 and 15). In case of Ce  $3d$  states we considered two additional peaks at  $\sim 892$  eV and  $\sim 916$  eV, while for Pr  $3d$  spectra additional peak at  $\sim 955$  eV was added. According to the literature, these additional structures may originate from different excitations, e.g. plasmon energy loss [?].

### 3.8. first-principles calculations

#### 3.8.1. Relativistic Atomic Energies

We start the theoretical analysis by presenting the widest range of the electronic structure for the representative composition  $CeCoGe_3$ . figure 17 shows the relativistic atomic energies on three successively decreasing ranges. The middle one can be compared with the measured XPS survey spectrum presented before. The atomic energies are attributed to particular orbitals, where the scales allow for it. The calculated positions of the energy states are in a good agreement with the XPS experimental results presented before.

#### 3.8.2. X-ray Photoelectron Spectra

The main purpose of our first-principles calculations is the interpretation of the measured XPS valence band spectra and investigations of magnetic properties. To this end, we prepare models of the most characteristic compositions  $CeCoGe_3$ ,  $Ce_{0.5}Pr_{0.5}CoGe_3$  and  $PrCoGe_3$  and determine for them the density of states and the spectra of X-ray photoelectrons.

The presence of  $4f$  elements in the system under consideration motivates us to go beyond LSDA formalism and apply the LSDA plus on-site repulsion term  $U$  (LSDA+ $U$ ) approach. For the reason that the on-site repulsion term  $U$  applied to Ce  $4f$  orbitals does not affect noticeably the part of the valence band located below the  $E_F$ , in our previous work on  $CeCoGe_3$  we presented only the XPS spectra

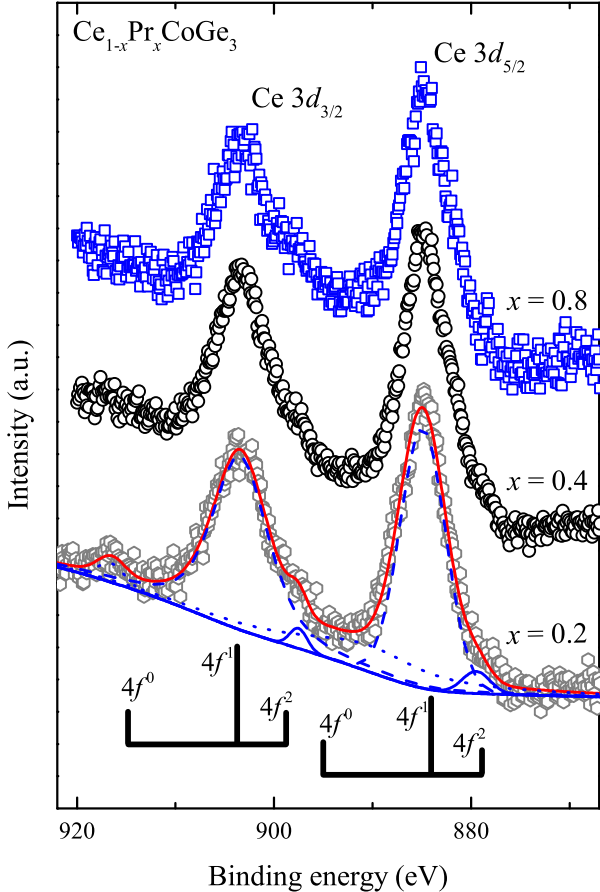


Figure 15: The Ce 3d XPS spectra for the  $\text{Ce}_{1-x}\text{Pr}_x\text{CoGe}_3$  samples. The spectral intensities are normalized to the intensity of the Ce  $3d_{5/2}$  peak. For selected sample,  $\text{Ce}_{0.8}\text{Pr}_{0.2}\text{CoGe}_3$ , the convolution of Ce 3d states is presented. Open symbol correspond to the experimental spectrum, while the lines to the fitting results (see text).

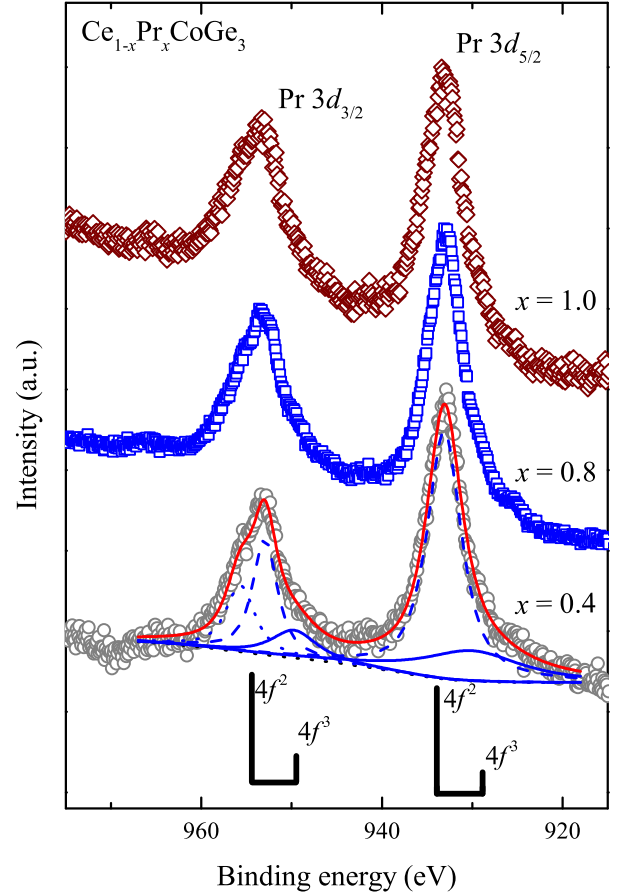


Figure 16: The Pr 3d XPS spectra for the  $\text{Ce}_{1-x}\text{Pr}_x\text{CoGe}_3$  samples. The spectral intensities are normalized to the intensity of the Pr  $3d_{5/2}$  peak. For selected sample,  $\text{Ce}_{0.6}\text{Pr}_{0.4}\text{CoGe}_3$ , the convolution of Pr 3d states is presented. Open symbol correspond to the experimental spectrum, while the lines to the fitting results (see text).

calculated without U [40]. However, because in contrast to the Ce case the on-site repulsion U applied to Pr 4f orbitals significantly affects the valence band below  $E_F$  we decide to consequently present all the calculated XPS spectra with taking into account the on-site repulsion term  $U_{4f}$  equal to 6 eV, see fig. 18. Comparison of the XPS spectra calculated for  $\text{CeCoGe}_3$ ,  $\text{Ce}_{0.5}\text{Pr}_{0.5}\text{CoGe}_3$  and  $\text{PrCoGe}_3$  shows that the bands between 0 and 6 eV consist mainly of Co 3d shares and a much smaller Ge 4p shares. With increasing Pr concentration the new maximum for Pr 4f is formed and develop at about 4 eV and at the same time the Ce 4f contribution observed on the Fermi level decreases. The main features of the calculated XPS spectra are in reasonable agreement with the experimental results shown before.

### 3.8.3. Charge Analysis

The Table 3 presents the excess electron numbers (resultant charges) calculated for  $\text{CeCoGe}_3$  and  $\text{PrCoGe}_3$ . For  $\text{CeCoGe}_3$  the resultant charge taken from Ce site (-1.23) is transferred to the Co (+0.17) and Ge (+0.47,

Table 3: Excess electron number (resultant charge) for  $\text{CeCoGe}_3$  and  $\text{PrCoGe}_3$  compounds, as calculated with the FPLO18 code using the PBE functional without spin polarization, treating the relativistic effects in a full 4-component formalism (including spin-orbit coupling) and taking into account an on-site repulsion term  $U_{4f}$  equal to 6 eV. The inequivalent atomic sites are considered according to Refs. [28, 46]. Unlike remaining sites, the multiplicity for Ge2 per formula unit is two instead of one.

formula/site	Ce/Pr	Co	Ge1	Ge2
$\text{CeCoGe}_3$	-1.23	0.17	0.47	0.30
$\text{PrCoGe}_3$	-1.16	0.18	0.43	0.27

+0.30) sites and a similar picture is observed for  $\text{PrCoGe}_3$ . Some more details about the orbital filling is provided from the Mulliken electronic population analysis [79], see Table 4. For Ce/Pr sites, we observe a slight depopulation of 5p orbitals and a low occupation of 6s and 6p orbitals. The large difference between the Ce and Pr electronic configuration is found for 4f orbitals (0.98 versus 2.15), which comes from the difference in atomic numbers of the ele-

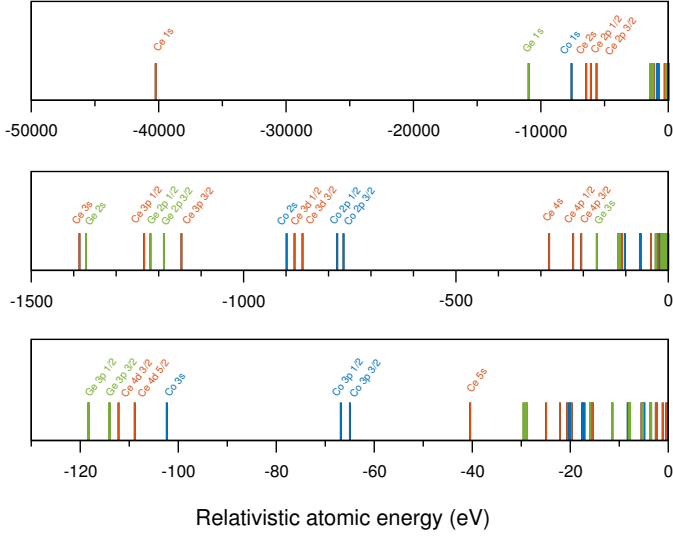


Figure 17: The relativistic atomic energies for CeCoGe<sub>3</sub> as calculated with the FPLO18 code using the PBE functional without spin polarization and treating the relativistic effects in a full 4-component formalism (including spin-orbit coupling).

Table 4: The Mulliken electronic population analysis for CeCoGe<sub>3</sub> and PrCoGe<sub>3</sub> compounds, as calculated with the FPLO18 code using the PBE functional without spin polarization, treating the relativistic effects in a full 4-component formalism (including spin-orbit coupling) and taking into account an on-site repulsion term  $U_{4f}$  equal to 6 eV. The inequivalent atomic sites are considered according to Refs. [28, 46]. Results for several almost empty valence orbitals are not presented, although they were included in the calculations.

	site	5p	6s	5d	6p	4f
CeCoGe <sub>3</sub>	Ce	5.82	0.19	1.59	0.14	0.98
PrCoGe <sub>3</sub>	Pr	5.73	0.25	1.50	0.22	2.15
	site	4s	3d	4d	4p	
CeCoGe <sub>3</sub>	Co	0.52	7.91	0.19	0.53	
PrCoGe <sub>3</sub>	Co	0.52	7.92	0.19	0.54	
	site	4s	4p	4d		
CeCoGe <sub>3</sub>	Ge1	1.60	2.71	0.16		
PrCoGe <sub>3</sub>	Ge1	1.59	2.53	0.17		
	site	4s	4p	4d		
CeCoGe <sub>3</sub>	Ge2	1.60	2.55	0.17		
PrCoGe <sub>3</sub>	Ge2	1.60	2.53	0.17		

ments. In case of Co sites we observe the depopulation of the 4s orbitals with a simultaneous increase in occupation of the 3d orbital, with respect to the electronic configuration of the ground state of a neutral Co atom ( $3d^7 4s^2$ ). In addition, the Co 4d and 4p orbitals become partially occupied. In the case of Ge sites we observe the accumulation

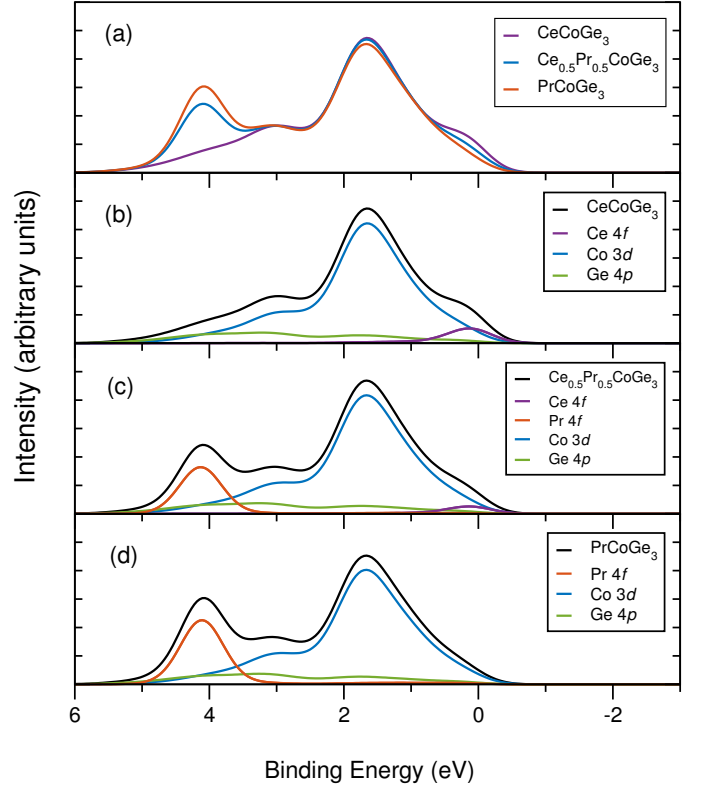


Figure 18: The valence band X-ray photoelectron spectra as calculated with the FPLO18 code using the PBE functional, treating the relativistic effects in a full 4-component formalism (including spin-orbit coupling), taking into account an on-site repulsion term  $U_{4f}$  equal to 6 eV and assuming lack of spin polarization. (a) Comparison of the results for CeCoGe<sub>3</sub>, Ce<sub>0.5</sub>Pr<sub>0.5</sub>CoGe<sub>3</sub> and PrCoGe<sub>3</sub>. (b, c, d) The most important contributions from individual orbitals compared to the total XPS spectra.

of charge on 4p and 4d orbitals and partial depopulation of 4s orbitals, with respect to the electronic configuration of the ground state of a neutral Ge atom ( $3d^{10} 4s^2 4p^2$ ). In summary, chemical bonds in CeCoGe<sub>3</sub> and PrCoGe<sub>3</sub> compounds result mainly from the interaction of Ce/Pr 5d, Co 3d, and Ge 4p and 4s orbitals.

#### 3.8.4. Magnetic properties

Our magnetic measurements presented before confirmed the observed previously appearance of three magnetic phase transitions at 21, 12 and 8 K for CeCoGe<sub>3</sub> [29]. They have been interpreted as the transitions between paramagnetic, ferrimagnetic, and antiferromagnetic configurations [28]. We also confirmed experimentally that the finding of lack of magnetic order in PrCoGe<sub>3</sub> [45]. Furthermore, for PrCoGe<sub>3</sub> it has been found previously that the magnetization in a magnetic field parallel to 001 direction indicates characteristic metamagnetic transition at 50 T [45]. Furthermore, our measurements indicated ordered magnetic ground state for Ce<sub>1-x</sub>Pr<sub>x</sub>CoGe<sub>3</sub> system with Pr concentration x up to about 0.6.

In order to investigate the magnetic properties of

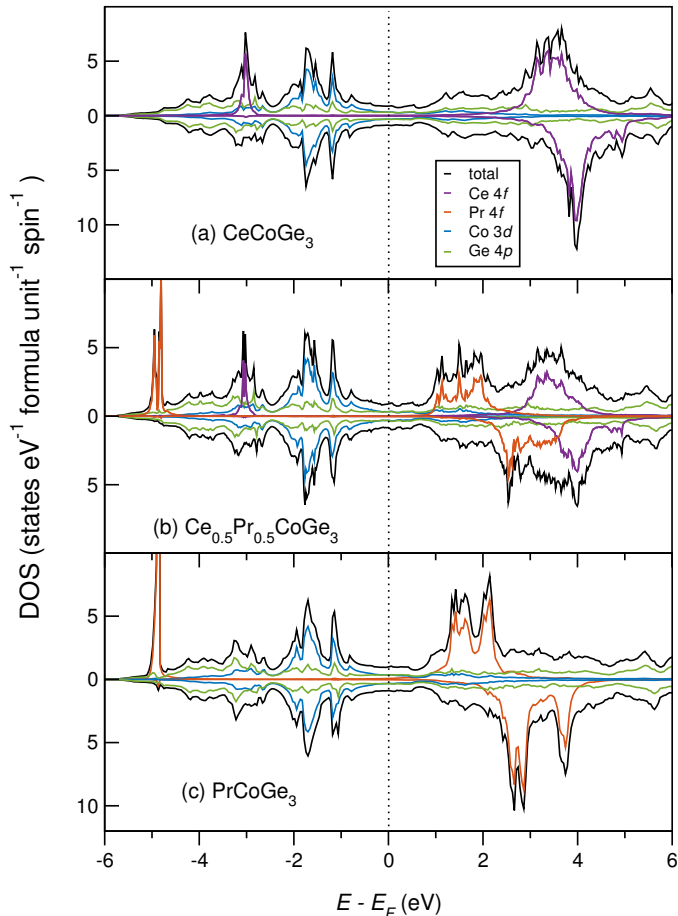


Figure 19: The densities of states (DOS) for  $\text{CeCoGe}_3$ ,  $\text{Ce}_{0.5}\text{Pr}_{0.5}\text{CoGe}_3$  and  $\text{PrCoGe}_3$  as calculated with the FPLO18 code using the PBE functional with spin polarization (parallel configuration of magnetic moments on  $4f$  sites), treating the relativistic effects in a full 4-component formalism (including spin-orbit coupling) and taking into account an on-site repulsion term  $U_{4f}$  equal to 6 eV. The most important contributions from individual orbitals are compared to the total DOS. For each composition, two spin channels are presented.

considered compositions, we decided to extend the non-magnetic first-principles investigations presented before into spin-polarized approach. We will show the results of spin-polarized calculations considering rather artificial simplified models of collinear parallel configurations of magnetic moments on  $4f$  elements with the magnetization axis pointing 001 direction. Hopefully, it will help to better understand the more complex non-collinear antiferromagnetic ground state of  $\text{CeCoGe}_3$  predicted experimentally [28] and difficult to reproduce theoretically within a common framework with full-potential full-relativistic model including on-site repulsion  $U$ .

Figure 19 shows the spin-polarized DOS together with the selected contributions of individual orbitals (Ce/Pr  $4f$ , Co  $3d$ , and Ge  $4p$ ). The observed hybridization between the Co  $3d$  and Ge  $4p$  orbitals confirms the formation of the  $3d-4p$  covalent bonds. Inclusion of spin-orbit coupling

leads to an image with  $4f$  states split into  $4f_{5/2}$  and  $4f_{7/2}$ . Moreover, the application of the on-site repulsion term  $U$  further separates the Ce  $4f$  states into parts below and above the Fermi level. The occupied  $4f$  states form the sharp peaks at about -3 eV (Ce) and -5 eV (Pr), which indicates their localized character. The image of DOS for the intermediate composition  $\text{Ce}_{0.5}\text{Pr}_{0.5}\text{CoGe}_3$  is similar to simple combination of terminal cases. The observed splitting of two spin channels is proportional to the spin magnetic moments and noticeably increases with Pr concentration.

Table 5: The spin, orbital, and total magnetic moments ( $\mu_B$  (atom or f.u.) $^{-1}$ ) for  $\text{CeCoGe}_3$ ,  $\text{Ce}_{0.5}\text{Pr}_{0.5}\text{CoGe}_3$  and  $\text{PrCoGe}_3$  as calculated with the FPLO18 code using the PBE functional, treating the relativistic effects in a full 4-component formalism (including spin-orbit coupling), taking into account an on-site repulsion term  $U_{4f}$  equal to 6 eV and assuming parallel configuration of magnetic moments on  $4f$  sites. The saturation magnetization  $M_S$  ( $\text{kA m}^{-1}$ ) is evaluated based on the total magnetic moments  $m$  and experimental parameters. The magnetic moments for Ge are below  $0.02 \mu_B/\text{atom}$  and are not presented in this table.

	$\text{CeCoGe}_3$		$\text{Ce}_{0.5}\text{Pr}_{0.5}\text{CoGe}_3$		$\text{PrCoGe}_3$	
site	$m_s$	$m_l$	$m_s$	$m_l$	$m_s$	$m_l$
Ce	1.00	-0.56	1.00	-0.56	–	–
Pr	–	–	2.06	-1.36	2.07	-1.42
Co	-0.04	0.00	-0.05	0.01	-0.03	0.00
$m$	0.39		0.52		0.60	
$M_S$	39		53		61	

The calculated magnetic moments are presented in Table 5. The spin magnetic moments on Ce ( $1.00 \mu_B$ ) and Pr ( $2.06 \mu_B$ ) are close to integers, which is related with the strong localization of occupied  $4f$  orbitals. The utilized full-relativistic approach allows us to calculate also the orbital contributions to the magnetic moments, which in case of  $f$ -electron systems are often substantial. In our case the opposite orbital magnetic moments on Ce ( $-0.56 \mu_B$ ) and Pr ( $-1.42 \mu_B$ ) significantly reduce the resultant total magnetic moments. Whereas, the total magnetic moment increases with Pr concentration from  $0.39 \mu_B/\text{formula unit}$  for  $\text{CeCoGe}_3$  up to  $0.60 \mu_B/\text{formula unit}$  for  $\text{PrCoGe}_3$ . The magnetic moments on other elements are very small in comparison to the ones on  $4f$  elements. Moments on Co are below  $-0.05 \mu_B/\text{atom}$  and opposite to moments on  $4f$  elements, whereas moments on Ge are below  $0.02 \mu_B/\text{atom}$ .

#### 4. Phase diagram

Based on the evolution of the phase transitions temperatures with the substitution level  $x$  a magnetic phase diagram is constructed (figure 20) for the series  $\text{Ce}_{1-x}\text{Pr}_x\text{CoGe}_3$ . Linear extrapolation of the magnetic phase ordering temperature  $T_1$  to 0 K gives a critical Pr concentration equal to  $x = 0.66$ . Alongside with a reduction of the magnetism, the system exhibits a decrease in

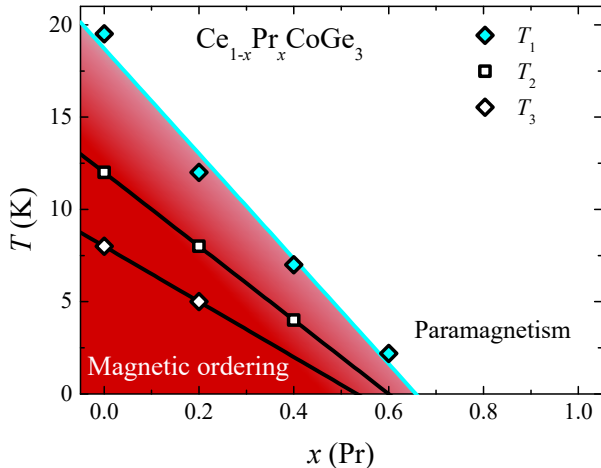


Figure 20: Magnetic phase diagram for the  $\text{Ce}_{1-x}\text{Pr}_x\text{CoGe}_3$  system. Data were obtained from the results of magnetic susceptibility. Solid lines are a linear extrapolation of specific phase transitions to a temperature of 0 K. Concentrations obtained for specific phase transitions: for  $T_1 - x = 0.66$ , for  $T_2 - x = 0.6$  and for  $T_3 - x = 0.53$ .

the strength of Kondo interaction. In terms of the Doniach diagram, we can assume that the system is approaching the low energy region of both interactions. This is a side opposite to the QCP region – increase in concentration  $x$  directs the diagram to a region with lower values of  $|JN_{\text{F}}|$ , therefore any possible NFL behaviour between concentration of  $x = 0.6$  and  $0.8$  would be connected with the formation of the Griffiths phase instead of the occurrence of the QCP. A possible explanation for the reduction of energy of both interactions may be related to the interference of both interactions due to the substitution of Pr for Ce in the crystal structure – the interactions have a specific range and placement of the Pr atom in the Ce site causes that the ranges of both interactions are too short to interact with the other nearest Ce atom. Considering that the  $\text{Pr}^{3+}$  ion has two entangled  $f$  electrons, the intriguing issue is also why praseodymium  $f$  electrons do not interact with the valence band. Hypothetically, to explain it, these two  $f$  electrons should have spin values of  $\frac{1}{2}$  and  $-\frac{1}{2}$ . This would lead to a state almost identical  $\text{La}^{3+}$  with the addition of two non-interactive  $f$  electrons. Moreover, this state of Pr has been indirectly confirmed by Kawai *et al.* [46], who has shown that the Fermi surface is identical for  $\text{PrCoGe}_3$  and  $\text{LaCoGe}_3$ . They have also confirmed that the  $f$  electrons contribute only to the cyclotron mass, which means that they are tightly entangled with the ion. A scenario with two opposing spins is possible if Hund’s rules are violated. This may occur due to a strong influence of CEF. Taking into account that the first CEF excitation is at low temperatures (visible as anomalies in all experimental results in temperature range of 10 – 30 K), this may be a reason for violation of Hund’s rules, resulting in two  $f$  electrons with different spins, because the low spin state is present.

## 5. Conclusions

We have presented results of various physical properties for the novel  $\text{Ce}_{1-x}\text{Pr}_x\text{CoGe}_3$  system, which shows the suppression of magnetic ordering with increasing  $x$  in isostructural transformation. From the magnetic hysteresis and  $MR$  measurements we deduced that the magnetic structure of the parent compound  $\text{CeCoGe}_3$  is preserved for a low content of Pr. In all presented experimental results, there is a significant contribution of CEF around temperature of 12 K, which can have a strong impact on the praseodymium state. In the studied alloys praseodymium behaves as lanthanum with two additional non-interactive  $f$  electron. More interestingly, the parent compound  $\text{PrCoGe}_3$  shows giant magnetoresistance, which is probably connected with the electronic band structure and reduced electrons mobility.

XPS measurements confirmed the successful synthesis of good quality samples of solid solutions for the  $\text{Ce}_{1-x}\text{Pr}_x\text{CoGe}_3$  series. Co  $2p$  spectra demonstrate the absence of contribution of Co oxides and a close similarity with Co metal. The Pr/Ce  $3d$  and  $4d$  XPS spectra point to a stable configuration of the Pr/Ce  $4f$  shell in studied materials. The stable valence 3 for Pr and Ce is consistent with X-ray diffraction data and magnetic susceptibility measurements.

We presented the results of first-principles calculations for  $\text{CeCoGe}_3$ ,  $\text{Ce}_{0.5}\text{Pr}_{0.5}\text{CoGe}_3$  and  $\text{PrCoGe}_3$ . We considered non-spin-polarized models as the basis for XPS spectra and spin-polarized models to investigate magnetic properties. We shown that substitution of Pr for Ce significantly affects the electronic structure of the alloys.

(1) The calculations explain the evolution with Pr concentration of the measured  $\text{Ce}_{1-x}\text{Pr}_x\text{CoGe}_3$  XPS spectra mainly as a change in the position and magnitude of  $4f$  contributions. (2) Mulliken electronic population analysis indicates electronic states of  $f$ -electron atoms as close to Ce  $f^1$  and Pr  $f^2$ . (3) The charge analysis and calculated densities of states indicate that the chemical bonds in  $\text{Ce}_{1-x}\text{Pr}_x\text{CoGe}_3$  alloys are mainly formed by Ce/Pr  $5d$ , Co  $3d$ , and Ge  $4p$  and  $4s$  orbitals. (4) The calculations indicate that charge transfer occurs mainly from  $4f$  elements towards Ge and Co sites.

The constructed magnetic phase diagram shows that the ordering temperature decreases monotonically with the increasing  $x$  and the extrapolation to 0 K provides  $x = 0.66$  for the phase transition  $T_1$ . The possibility of appearance of the NFL behaviour is very low, as the QCP scenario is excluded due to a reduction of energy of RKKY and Kondo interactions.

## Acknowledgments

MW acknowledges the financial support of the National Science Centre Poland under the decision DEC-2018/30/E/ST3/00267. Part of the computations was per-

formed on the resources provided by the Poznań Supercomputing and Networking Center (PSNC).

## References

- [1] P. Coleman, A. J. Schofield, Quantum criticality, *Nature* 433 (2005) 226.
- [2] M. B. Maple, R. E. Baumbach, N. P. Butch, J. J. Hamlin, M. Janoschek, Non-Fermi liquid regimes and superconductivity in the low temperature phase diagrams of strongly correlated  $d$ - and  $f$ -electron materials, *J. Low Temp. Phys.* 161 (2010) 4–54.
- [3] F. Steglich, S. Wirth, Foundations of heavy-fermion superconductivity: lattice Kondo effect and Mott physics, *Rep. Prog. Phys.* 79 (2016) 084502.
- [4] S. Wirth, F. Steglich, Exploring heavy fermions from macroscopic to microscopic length scales, *Nat. Rev. Materials* 1 (2016) 16051.
- [5] Z. Weng, M. Smidman, L. Jiao, X. Lu, H. Yuan, Multiple quantum phase transitions and superconductivity in Ce-based heavy fermions, *Rep. Prog. Phys.* 79 (2016) 094503.
- [6] M. Smidman, M. Salamon, H. Yuan, D. Agterberg, Superconductivity and spin-orbit coupling in non-centrosymmetric materials: a review, *Rep. Prog. Phys.* 80 (2017) 036501.
- [7] S. Doniach, The Kondo lattice and weak antiferromagnetism, *Physica B + C* 91 (1977) 231–234.
- [8] N. Kimura, K. Ito, K. Saitoh, Y. Umeda, H. Aoki, T. Terashima, Pressure-induced superconductivity in noncentrosymmetric heavy-fermion CeRhSi<sub>3</sub>, *Phys. Rev. Lett.* 95 (2005) 247004.
- [9] N. Kimura, K. Ito, H. Aoki, S. Uji, T. Terashima, Extremely high upper critical magnetic field of the noncentrosymmetric heavy fermion superconductor CeRhSi<sub>3</sub>, *Phys. Rev. Lett.* 98 (2007) 197001.
- [10] Y. Okuda, Y. Miyauchi, Y. Ida, Y. Takeda, C. Tonohiro, Y. Oduchi, T. Yamada, N. Duc Dung, T. D. Matsuda, Y. Haga, et al., Magnetic and superconducting properties of LaIrSi<sub>3</sub> and CeIrSi<sub>3</sub> with the non-centrosymmetric crystal structure, *J. Phys. Soc. Jpn.* 76 (2007) 044708.
- [11] A. Hillier, D. Adroja, P. Manuel, V. Anand, J. Taylor, K. McEwen, B. Rainford, M. Koza, Muon spin relaxation and neutron scattering investigations of the noncentrosymmetric heavy-fermion antiferromagnet CeRhGe<sub>3</sub>, *Phys. Rev. B* 85 (2012) 134405.
- [12] F. Honda, I. Bonalde, S. Yoshiuchi, Y. Hirose, T. Nakamura, K. Shimizu, R. Settai, Y. Ōnuki, Pressure-induced superconductivity in non-centrosymmetric compound CeIrGe<sub>3</sub>, *Physica C* 470 (2010) S543–S544.
- [13] M. Klicpera, P. Javorský, P. Čermák, A. Rudajevová, S. Daniš, T. Brunátová, I. Císařová, Crystal structure and its stability in CeCuAl<sub>3</sub> single crystal, *Intermetallics* 46 (2014) 126–130.
- [14] M. Klicpera, P. Javorský, P. Čermák, A. Schneidewind, B. Ouladdiaf, M. Diviš, Neutron scattering study of magnetic order in single-crystalline CeCuAl<sub>3</sub>, *Phys. Rev. B* 91 (2015) 224419.
- [15] D. Adroja, A. del Moral, C. de la Fuente, A. Fraile, E. Goremychkin, J. Taylor, A. Hillier, F. Fernandez-Alonso, Vibron Quasi-bound State in the Noncentrosymmetric Tetragonal Heavy-Fermion Compound CeCuAl<sub>3</sub>, *Phys. Rev. Lett.* 108 (2012) 216402.
- [16] H. Sugawara, S. Saha, T. Matsuda, Y. Aoki, H. Sato, J. Gavilano, H. Ott, Magnetic and transport properties in CeAuAl<sub>3</sub> single crystal, *Physica B* 259 (1999) 16–17.
- [17] D. Adroja, C. de la Fuente, A. Fraile, A. Hillier, A. Daoud-Aladine, W. Kockelmann, J. Taylor, M. Koza, E. Burzurí, F. Luis, et al., Muon spin rotation and neutron scattering study of the noncentrosymmetric tetragonal compound CeAuAl<sub>3</sub>, *Phys. Rev. B* 91 (2015) 134425.
- [18] C. Franz, A. Senyshyn, A. Regnat, C. Duvinage, R. Schönmann, A. Bauer, Y. Prots, L. Akselrud, V. Hlukhyy, V. Baran, et al., Single crystal growth of CeTAl<sub>3</sub> ( $T = \text{Cu, Ag, Au, Pd and Pt}$ ), *J. Alloy. Compd.* 688 (2016) 978–986.
- [19] D. Das, T. Gruner, H. Pfau, U. Paramanik, U. Burkhardt, C. Geibel, Z. Hossain, Heavy fermion and kondo lattice behavior in the itinerant ferromagnet CeCrGe<sub>3</sub>, *J. Phys.: Condens. Mat.* 26 (2014) 106001.
- [20] D. Das, S. Nandi, I. da Silva, D. Adroja, Z. Hossain, Neutron diffraction study on heavy-fermion compound CeCrGe<sub>3</sub>, *Phys. Rev. B* 94 (2016) 174415.
- [21] K. Synoradzki, D. Das, A. Frackowiak, D. Szymański, P. Skokowski, D. Kaczorowski, Study on magnetocaloric and thermoelectric application potential of ferromagnetic compound CeCrGe<sub>3</sub>, *J. Appl. Phys.* 126 (2019) 075114.
- [22] P. Manfrinetti, S. Dhar, R. Kulkarni, A. Morozkin, Crystal structure and the magnetic properties of CeTiGe<sub>3</sub>, *Solid State Commun.* 135 (2005) 444–448.
- [23] U. S. Kaluarachchi, V. Taufour, S. L. Bud’ko, P. C. Canfield, Quantum tricritical point in the temperature-pressure-magnetic field phase diagram of CeTiGe<sub>3</sub>, *Phys. Rev. B* 97 (2018) 045139.
- [24] M. Inamdar, A. Thamizhavel, S. Dhar, Anisotropic magnetic behavior of single crystalline CeTiGe<sub>3</sub> and CeVGe<sub>3</sub>, *J. Phys.: Condens. Mat.* 26 (2014) 326003.
- [25] W. Kittler, V. Fritsch, F. Weber, G. Fischer, D. Lamago, G. André, H. v. Löhneysen, Suppression of ferromagnetism of CeTiGe<sub>3</sub> by V substitution, *Phys. Rev. B* 88 (2013) 165123.
- [26] A. Pikul, D. Kaczorowski, T. Plackowski, A. Czopnik, H. Michor, E. Bauer, G. Hilscher, P. Rogl, Y. Grin, Kondo behavior in antiferromagnetic CeNiGe<sub>3</sub>, *Phys. Rev. B* 67 (2003) 224417.
- [27] M. Nakashima, K. Tabata, A. Thamizhavel, T. Kobayashi, M. Hedo, Y. Uwatoko, K. Shimizu, R. Settai, Y. Ōnuki, High-pressure effect on the electronic state in CeNiGe<sub>3</sub>: Pressure-induced superconductivity, *J. Phys.: Condens. Mat.* 16 (2004) L255.
- [28] V. Pecharsky, O.-B. Hyun, K. Gschneidner Jr, Unusual magnetic properties of the heavy-fermion compound CeCoGe<sub>3</sub>, *Phys. Rev. B* 47 (1993) 11839.
- [29] A. Thamizhavel, T. Takeuchi, T. D. Matsuda, Y. Haga, K. Sugiyama, R. Settai, Y. Ōnuki, Unique magnetic phases in an antiferromagnet CeCoGe<sub>3</sub>, *J. Phys. Soc. Jpn.* 74 (2005) 1858–1864.
- [30] S. Bud’ko, M. Fontes, S. De Medeiros, M. Continentino, E. Baggio-Saitovitch, Magnetoresistance in CeTGe<sub>3</sub> ( $T = \text{Fe, Co}$ ), *Physica B* 259 (1999) 118–120.
- [31] K. Kaneko, N. Metoki, T. Takeuchi, T. D. Matsuda, Y. Haga, A. Thamizhavel, R. Settai, Y. Ōnuki, Multi-step magnetic transition in non-centrosymmetric compound CeCoGe<sub>3</sub>, *J. Phys. Conf. Ser.* 150 (2009) 042082.
- [32] M. Smidman, D. Adroja, A. Hillier, L. Chapon, J. Taylor, V. Anand, R. P. Singh, M. Lees, E. Goremychkin, M. Koza, et al., Neutron scattering and muon spin relaxation measurements of the noncentrosymmetric antiferromagnet CeCoGe<sub>3</sub>, *Phys. Rev. B* 88 (2013) 134416.
- [33] T. Kawai, M. Nakashima, Y. Okuda, H. Shishido, T. Shimoda, T. D. Matsuda, Y. Haga, T. Takeuchi, M. Hedo, Y. Uwatoko, et al., Pressure Effect of Electronic States in Antiferromagnets CeTX<sub>3</sub> ( $t$ : Transition Metal,  $x$ : Si and Ge), *J. Phys. Soc. Jpn.* 76 (2007) 166–167.
- [34] R. Settai, I. Sugitani, Y. Okuda, A. Thamizhavel, M. Nakashima, Y. Ōnuki, H. Harima, Pressure-induced superconductivity in CeCoGe<sub>3</sub> without inversion symmetry, *J. Magn. Magn. Mater.* 310 (2007) 844–846.
- [35] V. Krishnamurthy, K. Nagamine, I. Watanabe, K. Nishiyama, S. Ohira, M. Ishikawa, D. Eom, T. Ishikawa, T. Briere, Non-Fermi-Liquid Spin Dynamics in CeCoGe<sub>3-x</sub>Si<sub>x</sub> for  $x = 1.2$  and  $1.5$ , *Phys. Rev. Lett.* 88 (2002) 046402.
- [36] K. Kanai, T. Terashima, D. Eom, M. Ishikawa, S. Shin, Observation of the coherence transition into a collective dense kondo state by resonant inverse photoemission spectroscopy, *Phys. Rev. B* 60 (1999) R9900.
- [37] J. Larrea J, J. Teyssier, H. Rønnow, K.-A. Lorenzer, S. Paschen, High pressure electrical resistivity and specific heat of the heavy fermion compound CeCoGe<sub>2.2</sub>Si<sub>0.8</sub>: Part of Special Issue on Quantum Criticality and Novel Phases, *Phys. Status Solidi B*

- 250 (2013) 511–514.
- [38] S. De Medeiros, S. Bud'ko, M. Fontes, M. Continentino, E. Baggio-Saitovitch, Phase diagram of  $\text{Ce}(\text{Co}_{1-x}\text{Fe}_x)\text{Ge}_3$ : from complex magnetic ordering to a non-magnetic Fermi liquid, *J. Magn. Magn. Mater.* 226 (2001) 152–154.
- [39] P. Skokowski, K. Synoradzki, T. Toliński, Magnetoresistance of the  $\text{CeCo}_{1-x}\text{Fe}_x\text{Ge}_3$  alloys, *Acta Phys. Pol. A* 10 (2017) 1000–1002.
- [40] P. Skokowski, K. Synoradzki, M. Werwiński, A. Bajorek, G. Chelkowska, T. Toliński, Electronic structure of  $\text{CeCo}_{1-x}\text{Fe}_x\text{Ge}_3$  studied by X-ray photoelectron spectroscopy and first-principles calculations, *J. Alloy. Compd.* 787 (2019) 744–750.
- [41] O. Bednarchuk, D. Kaczorowski, Low-temperature physical properties of single-crystalline  $\text{EuCoGe}_3$  and  $\text{EuRhGe}_3$ , *Acta Phys. Pol. A* 127 (2015) 418–420.
- [42] O. Bednarchuk, A. Gator, D. Kaczorowski, Synthesis, crystal structure and physical properties of  $\text{EuTGe}_3$  ( $T = \text{Co}, \text{Ni}, \text{Rh}, \text{Pd}, \text{Ir}, \text{Pt}$ ) single crystals, *J. Alloy. Compd.* 622 (2015) 432–439.
- [43] M. Kakihana, H. Akamine, K. Tomori, K. Nishimura, A. Teruya, A. Nakamura, F. Honda, D. Aoki, M. Nakashima, Y. Amako, et al., Superconducting, Fermi surface, and magnetic properties in  $\text{SrTGe}_3$  and  $\text{EuTGe}_3$  ( $T$ : Transition metal) with the Rashba-type tetragonal structure, *J. Alloy. Compd.* 694 (2017) 439–451.
- [44] Y. Utsumi, D. Kasinathan, P. Swatek, O. Bednarchuk, D. Kaczorowski, J. M. Ablett, J.-P. Rueff, Bulk electronic structure of non-centrosymmetric  $\text{EuTGe}_3$  ( $T = \text{Co}, \text{Ni}, \text{Rh}, \text{Ir}$ ) studied by hard X-ray photoelectron spectroscopy, *Phys. Rev. B* 97 (2018) 115155.
- [45] M.-a. Méasson, H. Muranaka, T. Kawai, Y. Ota, K. Sugiyama, M. Hagiwara, K. Kindo, T. Takeuchi, K. Shimizu, F. Honda, et al., Magnetic properties of  $\text{RCoGe}_3$  ( $R$ : Ce, Pr, and Nd) and strong anisotropy of the upper critical field in non-centrosymmetric compound  $\text{CeCoGe}_3$ , *J. Phys. Soc. Jpn.* 78 (2009) 124713.
- [46] T. Kawai, H. Muranaka, T. Endo, N. D. Dung, Y. Doi, S. Ikeda, T. D. Matsuda, Y. Haga, H. Harima, R. Settai, et al., Split Fermi surface properties of  $\text{LaTGe}_3$  ( $T$ : transition metal) and  $\text{PrCoGe}_3$  with the non-centrosymmetric crystal structure, *J. Phys. Soc. Jpn.* 77 (2008) 064717–064717.
- [47] D. Eom, M. Ishikawa, J. Kitagawa, N. Takeda, Suppression of Antiferromagnetism by Kondo Effect and Quantum Critical Behavior in  $\text{CeCoGe}_{3-x}\text{Si}_x$  ( $0 \leq x \leq 3$ ), *J. Phys. Soc. Jpn.* 67 (1998) 2495–2500.
- [48] K. Koepnik, H. Eschrig, Full-potential nonorthogonal local-orbital minimum-basis band-structure scheme, *Phys. Rev. B* 59 (1999) 1743–1757.
- [49] K. Momma, F. Izumi, *VESTA*: A three-dimensional visualization system for electronic and structural analysis, *J. Appl. Crystallogr.* 41 (2008) 653–658.
- [50] J. P. Perdew, K. Burke, M. Ernzerhof, Generalized gradient approximation made simple, *Phys. Rev. Lett.* 77 (1996) 3865–3868.
- [51] E. R. Ylvisaker, W. E. Pickett, K. Koepnik, Anisotropy and magnetism in the LSDA +  $U$  method, *Phys. Rev. B* 79 (2009) 035103.
- [52] M. T. Czyżyk, G. A. Sawatzky, Local-density functional and on-site correlations: The electronic structure of  $\text{La}_2\text{CuO}_4$  and  $\text{LaCuO}_3$ , *Phys. Rev. B* 49 (1994) 14211.
- [53] V. I. Anisimov, O. Gunnarsson, Density-functional calculation of effective Coulomb interactions in metals, *Phys. Rev. B* 43 (1991) 7570–7574.
- [54] F. Tran, J. Schweifer, P. Blaha, K. Schwarz, P. Novák, PBE +  $U$  calculations of the Jahn-Teller effect in  $\text{Pr O}_2$ , *Phys. Rev. B* 77.
- [55] C. Morice, E. Artacho, S. E. Dutton, H.-J. Kim, S. S. Saxena, Electronic and magnetic properties of superconducting  $\text{LnO}_{1-x}\text{F}_x\text{BiS}_2$  ( $\text{Ln} = \text{La}, \text{Ce}, \text{Pr}, \text{and Nd}$ ) from first principles, *J. Phys. Condens. Matter* 28 (2016) 345504.
- [56] J. J. Yeh, I. Lindau, Atomic subshell photoionization cross sections and asymmetry parameters:  $1 \leq Z \leq 103$ , *At. Data Nucl. Data Tables* 32 (1985) 1–155.
- [57] J. Rodríguez-Carvajal, Recent advances in magnetic structure determination by neutron powder diffraction, *Physica B* 192 (1993) 55–69.
- [58] P. Skokowski, K. Synoradzki, T. Toliński, Comprehensive studies of the transformation between antiferromagnetic  $\text{CeCoGe}_3$  and heavy fermion  $\text{CeFeGe}_3$  compounds, *J. Alloy. Compd.* 810 (2019) 151850.
- [59] T. Toliński, M. Falkowski, K. Synoradzki, A. Hoser, N. Stüßer, Magnetocaloric effect in the ferromagnetic  $\text{GdNi}_4\text{M}$  ( $M = \text{Al}, \text{Si}$ ) and antiferromagnetic  $\text{NdNiAl}_4$  compounds, *J. Alloy. Compd.* 523 (2012) 43–48.
- [60] B. Banerjee, On a generalised approach to first and second order magnetic transitions, *Phys. Lett.* 12 (1964) 16–17.
- [61] T. Toliński, K. Synoradzki, Spin-glass behavior in  $\text{CeCu}_x\text{Ni}_{4-x}\text{Mn}$  and  $\text{Ce}_{0.9}\text{Nd}_{0.1}\text{Ni}_4\text{Mn}$  compounds, *Intermetallics* 19 (2011) 62–67.
- [62] C. Rotundu, K. Ingersent, B. Andracka, Crystalline electric field contribution to the magnetoresistance of  $\text{Pr}_{1-x}\text{La}_x\text{Os}_4\text{Sb}_{12}$ , *Phys. Rev. B* 75 (2007) 104504.
- [63] C. Mazumdar, A. Nigam, R. Nagarajan, C. Godart, L. Gupta, B. Padalia, G. Chandra, R. Vijayaraghavan, Positive giant magnetoresistance in antiferromagnetic  $\text{RE}_2\text{Ni}_3\text{Si}_5$  ( $\text{RE} = \text{Tb}, \text{Sm}, \text{Nd}$ ), *Appl. Phys. Lett.* 68 (1996) 3647–3649.
- [64] V. Anand, Z. Hossain, C. Geibel, Magnetic and transport properties of  $\text{PrTGe}_3$  ( $T = \text{Ni}, \text{Rh}$ ), *Solid State Commun.* 146 (2008) 335–339.
- [65] A. Das, A. Nigam, Resistivity and magnetoresistance studies on  $\text{RCoGe}_3$  ( $R = \text{La}, \text{Ce}$ ) compounds, *J. Phys.: Condens. Mat.* 12 (2000) 1315.
- [66] B. Penc, D. Kaczorowski, A. Szytuła, A. Winiarski, A. Zarzycki, Magnetic properties and electronic structure of  $\text{R}_3\text{T}_4\text{X}_4$  compounds ( $R = \text{Pr}, \text{Nd}; T = \text{Cu}, \text{Ag}; X = \text{Ge}, \text{Sn}$ ), *Intermetallics* 15 (2007) 1489–1496.
- [67] Y. Baer, R. Hauger, C. Zürcher, M. Campagna, G. Wertheim, X-ray photoemission study of Ce-pnictides, *Phys. Rev. B* 18 (1978) 4433.
- [68] K. Synoradzki, T. Toliński, G. Chelkowska, A. Bajorek, M. Zapotoková, M. Reiffers, A. Hoser, X-ray photoemission, calorimetric, and electrical transport properties of  $\text{CeCu}_4\text{Mn}_y\text{Al}_{1-y}$ , *J. Alloy. Compd.* 601 (2014) 43–49.
- [69] T. Toliński, K. Synoradzki, A. Bajorek, G. Chelkowska, M. Koterlyn, G. Koterlyn, R. Yasnitskii, Influence of chemical composition on the X-ray photoemission, thermopower, specific heat, and magnetic properties of  $\text{CeNi}_2(\text{Si}_{1-y}\text{Ge}_y)_2$ , *Appl. Phys. A* 123 (2017) 408.
- [70] M. C. Biesinger, B. P. Payne, A. P. Grosvenor, L. W. Lau, A. R. Gerson, R. S. C. Smart, Resolving surface chemical states in XPS analysis of first row transition metals, oxides and hydroxides: Cr, Mn, Fe, Co and Ni, *Appl. Surf. Sci.* 257 (2011) 2717–2730.
- [71] A. Ohta, T. Fujioka, H. Murakami, S. Higashi, S. Miyazaki, X-ray photoelectron spectroscopy study of interfacial reactions between metal and ultrathin Ge oxide, *Jpn. J. Appl. Phys.* 50 (2011) 10PE01.
- [72] S. Lütkehoff, M. Neumann, A. Ślebarski,  $3d$  and  $4d$  X-ray-photoelectron spectra of Pr under gradual oxidation, *Phys. Rev. B* 52 (1995) 13808.
- [73] A. Ślebarski, M. Neumann, S. Mähl, Electronic structure of Pr in  $\text{PdPr}_{0.014}$ , *Phys. Rev. B* 51 (1995) 11113.
- [74] A. Ślebarski, A. Jezierski, A. Zygmunt, M. Neumann, S. Mähl, G. Borstel, The crystallographic, magnetic and electronic properties of  $\text{RM}_2\text{X}_2$  ( $R = \text{La}, \text{Ce}, \text{Pr}; M = \text{Cu}, \text{Ni}; X = \text{Sn}, \text{Sb}$ ), *J. Magn. Magn. Mater.* 159 (1996) 179–191.
- [75] O. Gunnarsson, K. Schönhammer, Electron spectroscopies for Ce compounds in the impurity model, *Phys. Rev. B* 28 (1983) 4315.
- [76] H. Ogasawara, A. Kotani, B. T. Thole, Lifetime effect on the multiplet structure of  $4d$  X-ray-photoemission spectra in heavy rare-earth elements, *Phys. Rev. B* 50 (1994) 12332.

- [77] S. Tougaard, P. Sigmund, Influence of elastic and inelastic scattering on energy spectra of electrons emitted from solids, *Phys. Rev. B* 25 (1982) 4452.
- [78] A. Yamasaki, S. Imada, A. Sekiyama, M. Tsunekawa, C. Dallera, L. Braicovich, T.-L. Lee, H. Sugawara, H. Sato, R. Settai, et al., Bulk-sensitive photoemission spectroscopy for heavy-fermion Pr compounds using hard X-ray, *J. Phys. Soc. Jpn.* 74 (2005) 2045–2051.
- [79] R. S. Mulliken, Electronic Population Analysis on LCAO–MO Molecular Wave Functions. I, *J. Chem. Phys.* 23 (1955) 1833–1840.